

The Pennsylvania State University
The Graduate School
Department of Mechanical and Nuclear Engineering

**CORE-FREE ROLLED ACTUATORS FOR BRAILLE DISPLAYS
USING ELECTROSTRICTIVE P(VDF-TrFE-CFE) TERPOLYMER**

A Thesis in
Mechanical Engineering

by
Thomas Levard

© 2011 Thomas Levard

Submitted in Partial Fulfillment
of the Requirements
for the Degree of

Master of Science

May 2011

The thesis of Thomas Levard was reviewed and approved* by the following:

Christopher D. Rahn
Professor of Mechanical Engineering
Thesis Co-Advisor

Qiming Zhang
Distinguished Professor of Electrical Engineering
Thesis Co-Advisor

Amanul Haque
Associate Professor of Mechanical Engineering

Karen A. Thole
Professor of Mechanical Engineering
Head of the Department of Department or Graduate Program

*Signatures are on file in the Graduate School

ABSTRACT

Refreshable Braille displays require many, small diameter actuators to move the pins. The electrostrictive P(VDF-TrFE-CFE) terpolymer can provide the high strain and actuation force under modest electric fields that are required of this application. In this thesis, we develop core-free tubular actuators and integrate them into a 3×2 Braille cell. The films are solution cast, stretched to $6 \mu\text{m}$ thick, electroded, laminated into a bilayer, rolled into a 2 mm diameter tube, bonded, and provided with top and bottom contacts. Experimental testing of 17 actuators demonstrates significant strains (up to 4%) and blocking forces (1 N) at moderate electric fields (100 MV/m). A novel Braille cell is designed and fabricated using six of these actuators.

TABLE OF CONTENTS

LIST OF FIGURES	v
LIST OF TABLES.....	ix
Chapter 1 Introduction	1
Chapter 2 Actuator Design.....	3
Concept.....	3
Design.....	4
Chapter 3 Fabrication Process	6
Solution Casting.....	6
Stretching and Annealing	6
Electrode Deposition	7
Lamination.....	8
Rolling	9
Bonding and Electrical Contact	10
Chapter 4 Experiments.....	11
Experimental Set up	11
Electrical Measurements.....	13
Strain Results	13
Force Results.....	16
Self Healing	18
Frequency Response and Cycle Life	20
Chapter 5 Braille Cell Design.....	21
Chapter 6 Conclusion and Future Work.....	23
References	25
Appendix A Capacitance and Loss data of the PVDF single layers.....	28
Appendix B Capacitance and Loss data of the PVDF bilayers.....	29
Appendix C Displacement data of the PVDF actuators.....	30
Appendix D Force data of the PVDF actuators.....	49
Appendix E Hysteresis and frequency response data of the PVDF actuators	59
Appendix F Temperature dependence data of the PVDF actuators	64

LIST OF FIGURES

Figure 2.1 Actuator and Braille Cell Design: (a) Rolled actuator concept (close-up inset shows four offset electrodes) and (b) Braille cell.....	4
Figure 3.1 PVDF film tensioned on a supporting frame with CPS and gold electrodes.	8
Figure 3.2 Bilayer lamination with electrodes on (a) 4 sides and (b) 3 sides.	9
Figure 3.3 Automated mandrel for the rolling process.....	10
Figure 3.4 An example core-free rolled P(VDF-CFE-TrFE) actuator.	10
Figure 4.1 Displacement and force measurement set up. (1) Laser vibrometer. (2) Load cell. (3) Actuator. (4) Supporting acrylic block. (5) High voltage input. (6) Ground. (7) Golden oil supply.....	12
Figure 4.2 Experimental time response for an example actuator: (a) Voltage, (b) Current, and (c) Displacement.....	15
Figure 4.3 Experimentally measured strain versus electric field for 17 actuators (blue diamond is the mean value and error bars indicate \pm one standard deviation).	16
Figure 4.4 Experimental time response for blocking force tests: (a) Voltage and (b) Blocking force.....	17
Figure 4.5 Average blocking force versus electric field for 8 actuators (blue diamond is the mean value and error bars indicate \pm one standard deviation).....	18
Figure 4.6 Self-healing effect in PVDF terpolymer.....	19
Figure 4.7 Experimental self-healing event time response: (a) Voltage, (b) Current, and (c) Displacement.	19
Figure 5.1 Picture of the Braille cell with close-up views of the six pins spelling ‘PSU’.....	22
Figure C.1 Displacement characteristics of actuator #1 for voltages ranging from 200V to 750V. (a) Voltage vs. time. (b) Current vs. time. (c) Displacement vs. time.	31
Figure C.2 Displacement characteristics of actuator #2 for voltages ranging from 200V to 750V. (a) Voltage vs. time. (b) Current vs. time. (c) Displacement vs. time.	32

Figure C.3 Displacement characteristics of actuator #3 for voltages ranging from 200V to 600V. (a) Voltage vs. time. (b) Current vs. time. (c) Displacement vs. time.	33
Figure C.4 Displacement characteristics of actuator #4 for voltages ranging from 200V to 700V. (a) Voltage vs. time. (b) Current vs. time. (c) Displacement vs. time.	34
Figure C.5 Displacement characteristics of actuator #5 for voltages ranging from 200V to 700V. (a) Voltage vs. time. (b) Current vs. time. (c) Displacement vs. time.	35
Figure C.6 Displacement characteristics of actuator #6 for voltages ranging from 200V to 650V. (a) Voltage vs. time. (b) Current vs. time. (c) Displacement vs. time.	36
Figure C.7 Displacement characteristics of actuator #7 for voltages ranging from 200V to 600V. (a) Voltage vs. time. (b) Current vs. time. (c) Displacement vs. time.	37
Figure C.8 Displacement characteristics of actuator #8 for voltages ranging from 200V to 550V. (a) Voltage vs. time. (b) Current vs. time. (c) Displacement vs. time.	38
Figure C.9 Displacement characteristics of actuator #9 for voltages ranging from 200V to 650V. (a) Voltage vs. time. (b) Current vs. time. (c) Displacement vs. time.	39
Figure C.10 Displacement characteristics of actuator #10 for voltages ranging from 200V to 750V. (a) Voltage vs. time. (b) Current vs. time. (c) Displacement vs. time.	40
Figure C.11 Displacement characteristics of actuator #11 for voltages ranging from 200V to 600V. (a) Voltage vs. time. (b) Current vs. time. (c) Displacement vs. time.	41
Figure C.12 Displacement characteristics of actuator #12 for voltages ranging from 200V to 850V. (a) Voltage vs. time. (b) Current vs. time. (c) Displacement vs. time.	42
Figure C.13 Displacement characteristics of actuator #13 for voltages ranging from 200V to 600V. (a) Voltage vs. time. (b) Current vs. time. (c) Displacement vs. time.	43
Figure C.14 Displacement characteristics of actuator #14 for voltages ranging from 200V to 700V. (a) Voltage vs. time. (b) Current vs. time. (c) Displacement vs. time.	44

Figure C.15 Displacement characteristics of actuator #15 for voltages ranging from 200V to 500V. (a) Voltage vs. time. (b) Current vs. time. (c) Displacement vs. time.	45
Figure C.16 Displacement characteristics of actuator #16 for voltages ranging from 200V to 700V. (a) Voltage vs. time. (b) Current vs. time. (c) Displacement vs. time.	46
Figure C.17 Displacement characteristics of actuator #17 for voltages ranging from 200V to 1050V. (a) Voltage vs. time. (b) Current vs. time. (c) Displacement vs. time.	47
Figure C.18 Strain characteristics of all 17 actuators as a function of the applied electric field.	48
Figure D.1 Force characteristics of actuator #2 for voltages ranging from 200V to 500V. (a) Voltage vs. time. (b) Force vs. time.	50
Figure D.2 Force characteristics of actuator #7 for voltages ranging from 200V to 600V. (a) Voltage vs. time. (b) Force vs. time.	51
Figure D.3 Force characteristics of actuator #9 for voltages ranging from 200V to 600V. (a) Voltage vs. time. (b) Force vs. time.	52
Figure D.4 Force characteristics of actuator #10 for voltages ranging from 200V to 700V. (a) Voltage vs. time. (b) Force vs. time.	53
Figure D.5 Force characteristics of actuator #12 for voltages ranging from 200V to 700V. (a) Voltage vs. time. (b) Force vs. time.	54
Figure D.6 Force characteristics of actuator #14 for voltages ranging from 200V to 600V. (a) Voltage vs. time. (b) Force vs. time.	55
Figure D.7 Force characteristics of actuator #16 for voltages ranging from 200V to 700V. (a) Voltage vs. time. (b) Force vs. time.	56
Figure D.8 Force characteristics of actuator #17 for voltages ranging from 200V to 600V. (a) Voltage vs. time. (b) Force vs. time.	57
Figure D.9 Force characteristics of all 8 actuators as a function of the applied electric field.	58
Figure E.1 Hysteresis characteristic of actuator #9 at 400 V and 0.1 Hz input sine wave.	59
Figure E.2 Hysteresis characteristic of actuator #9 at 400 V and 0.25 Hz input sine wave.	60

Figure E.3 Hysteresis characteristic of actuator #9 at 400 V and 0.5 Hz input sine wave.	60
Figure E.4 Hysteresis characteristic of actuator #9 at 400 V and 1 Hz input sine wave.	61
Figure E.5 Hysteresis characteristic of actuator #9 at 400 V and 2 Hz input sine wave.	61
Figure E.6 Hysteresis characteristic of actuator #9 at 400 V and 5 Hz input sine wave.	62
Figure E.7 Hysteresis characteristic of actuator #9 at 400 V and 10 Hz input sine wave.	62
Figure E.8 Frequency response of actuator #9 at 400 V.	63
Figure F.1 Displacement characteristics of actuator #16 at 400V as a function of temperature.	64

LIST OF TABLES

Table 4.1 P(VDF-TrFE-CFE) actuator properties	12
Table A.1 Electrode spraying data for single layers of P(VDF-TrFE-CFE) blends.....	28
Table B.1 Electrode spraying data for bilayers of P(VDF-TrFE-CFE) blends.....	29

ACKNOWLEDGEMENTS

First of all, I would like to thank my advisor, Dr. Christopher Rahn, for giving me the opportunity to work on this project, and for his help and guidance throughout my master's degree. His involvement largely contributed to the success of this adventure.

A special thanks to Paul Diglio, my partner on this project and best friend, who kept me motivated during those two years: we can be proud of what we have achieved.

I would also like to thank Dr. Qiming Zhang and his lab (Lee, David, Minren and Yu) for their expertise in the field, as well as providing quality film to work with.

Last, but not least, I would like to thank all the people that supported me while working towards my degree: my family back home, my labmates (Amir, Deepak, Hareesh, Kiron, Lloyd and Ying), and of course my friends here at Penn State whom I shared great moments with!

Chapter 1

Introduction

The development of a full page refreshable Braille display requires many, small diameter actuators to move the pins. Commercially available displays are expensive, bulky and limited to two lines of Braille characters. The piezoelectric bending actuators used in these devices require a significantly larger area than the Braille pins themselves. Designing a more compact, portable system would enable the blind community to interface freely with computers, and have access to new technologies such as the internet and e-mails.

The recent advancements in the field of Electro Active Polymers (EAPs) make those materials a promising solution for tactile display applications¹. The main challenge resides in designing a miniature actuator that can meet both the Braille displacement and force requirements while operating at low voltage. The designs that have been investigated include multilayer stacked actuators that contract^{2,3}, bistable electroactive polymers that use temperature control⁴, dielectric elastomer membranes that buckle^{5,6}, and PVDF bending bimorph actuators coupled with hydraulic fluids⁷.

Compared with other actuator materials, the electrostrictive P(VDF-TrFE) based terpolymers and its blends offer several unique advantages including large transverse electrostrictive strains (~5%) and high elastic modulus (~1GPa) which can be exploited for compact actuation devices^{8,9,10}. These actuator polymers can be fabricated into thin films (down to 1 μm) enabling low operation voltages for practical commercial devices.

Tubular actuators are commonly used as artificial muscles^{11,12,13,14,15,16}, but have not been considered for tactile devices. Their large diameter and soft structure, usually requiring internal

support springs, make them unsuitable for Braille applications. In this thesis, we present a new rolled actuator that meets all Braille display specifications and the corresponding fabrication process. Seventeen actuators made from P(VDF-TrFE-CFE), a ferroelectric polymer, are tested experimentally and a cell containing six Braille characters is successfully demonstrated.

Chapter 2

Actuator Design

The design of the actuator is driven by three major constraints: the necessity of a compact form factor, as well as providing the required displacement and blocking force for Braille applications. In this section, the concept of the core-free rolled actuator is presented, and then strain and stress equations are used to dimensionalize the actuator.

Concept

Figure 2.1 shows a schematic diagram of the P(VDF-TrFE-CFE) cylindrical actuators developed in this thesis. They consist of an electroded bilayer film that is rolled into a tube. An external electric field causes the film to contract through the thickness and extend longitudinally in the actuation direction. The positive and negative electrodes are offset, allowing an electrical contact at each end of the actuator. The number of layers, diameters, and length of the actuator are designed to avoid buckling under maximum blocking force. This means that the actuator does not need an internal core, setting it apart from existing devices. The P(VDF-TrFE-CFE) ferroelectric polymer used in this application provides large electrostrictive strain¹⁷ (3.5% at 100 MV/m) and high modulus ($\sim 10^9$ N/m²) for an easily read display.

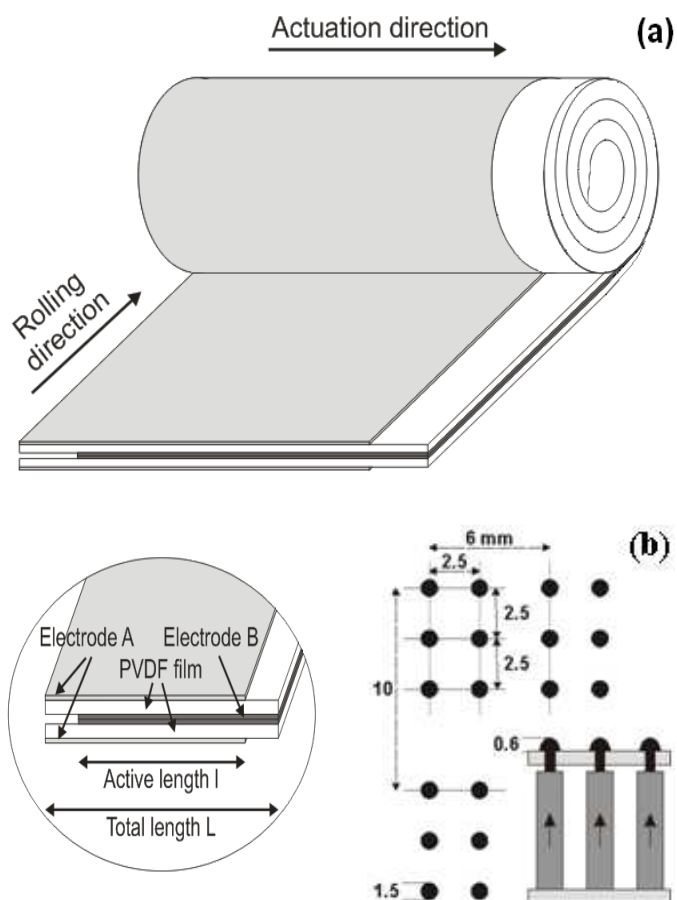


Figure 2.1 Actuator and Braille Cell Design: (a) Rolled actuator concept (close-up inset shows four offset electrodes) and (b) Braille cell.

Design

The dimensions of the roll actuator are based on a standard Braille cell¹⁸, shown in Fig. 2.1(b). The center-to-center distance between two adjacent dots is 2.5 mm, and the tip displacement must exceed 0.5 mm while withstanding a minimum force of 0.5 N. The blocking force and free stroke of the actuator at the maximum operating voltage are designed to satisfy these specifications.

The actuator displacement

$$\Delta = l\varepsilon,$$

where l is the active length of the actuator and ε is the strain at the applied voltage. The blocking force is

$$P = 2EtW\varepsilon$$

where t and W are respectively the thickness and rolling width of the single layer film, and E is the Young's modulus of the material in the axial direction (0.8 GPa).

The actuation voltage is chosen to provide an electric field of 100 MV/m and a corresponding strain of 3.5% without causing film breakdown. The average thickness of PVDF films is 6 μm so the actuation voltage is 600 V. With 3.5% strain an active length of 15 mm provides the required 0.5 mm pin displacement. To account for manufacturing and material variability, a length of 30 mm is used.

To enable a simple, core-free design, the actuator must be structurally stable under the applied blocking force. Due to the large length/diameter ratio, Euler buckling is the most likely failure mode. The critical buckling load

$$P_c = \frac{\pi EtW(\pi r_o^2 - tW)}{(kL)^2},$$

where L is the total length of the actuator, r_o is the outer diameter, and k accounts for boundary conditions¹⁹. In this analysis, we take $k = 1$, the worst case of pinned at both ends.

With $\pi r_o^2 \gg tW$, the maximum buckling load is reached when r_o and W are the largest and L is the smallest. For the Braille actuator, $L = 30$ mm and $t = 6$ μm . The fabrication process and cell design constrain 1.6 mm $< r_o < 2.2$ mm and 40 mm $< W < 75$ mm. If we pick the largest $r_o = 2.2$ mm and $W = 75$ mm, the maximum buckling load achievable is 9 N, corresponding to $\varepsilon = 1.5$ %. Thus, the actuator is prone to buckling and needs transverse support in the Braille cell design.

Chapter 3

Fabrication Process

A fabrication process is developed to perform the necessary steps in the making of the rolled actuator, starting from pure PVDF powder. The process involves solution casting, stretching, annealing, electrode deposition, lamination, rolling and bonding. The procedure is detailed hereafter.

Solution Casting

The polymer films are created using a solution blending and casting technique. PVDF powder mixed with CFE and TrFE are dissolved in a heated solvent solution. The solution is poured onto a glass substrate, left at rest for 12 hours, and then placed in a conventional oven and then a vacuum oven above room temperature ($\sim 80^{\circ}\text{C}$) to eliminate any remaining solvent. Finally, the film is removed from the glass substrate using deionized water. This method is very cost effective and simple but it creates film with randomly oriented polymer chains. To maximize actuation strain, the polymer chains are aligned using a stretching process.

Stretching and Annealing

After the casting process, the P(VDF-TrFE-CFE) film thickness is typically between 50 and 70 μm . To reduce the actuation voltage the samples are stretched down to a thickness of 6 μm . Stretching also aligns the polymer chains in the actuation direction, improving strain performance. Using either a linear or roll-to-roll stretching machine, the film, pulled in tension at

both ends, is locally heated with a hot wire, allowing the film to stretch according to a user defined ratio.

The abrupt change in temperature near the hot wire creates residual stresses in the stretched film. Annealing relaxes the film by heating close to the melting temperature followed by slow cooling. Annealing also increases the crystalline phase content, which contributes to the electrostrictive strain and improves the elastic modulus.

Electrode Deposition

For the electrode deposition step, the film is tensioned onto 7.5 cm by 10 cm metal frames using a repositionable spray adhesive as shown in Fig. 3.1. A mask is temporarily placed on top of the frame, delimiting an electrode pattern of 30 mm by 75 mm. A Conductive Polymer Solution (CPS – ClevosTM FE-T) was used as the electrode (blue area on film in Fig. 2). CPS is deposited onto the film using an ultrasonic nozzle (Sonaer 130K50T). The electrode performance (conductivity and capacitance, see Appendix A) increases with increasing electrode thickness but the strain performance degrades due to the additional passive constraint on displacement. The CPS spray time is adjusted to balance these opposing objectives. A thin gold layer is also deposited on the edge of the electrode pattern, to improve electrical contact at the ends of the actuator.

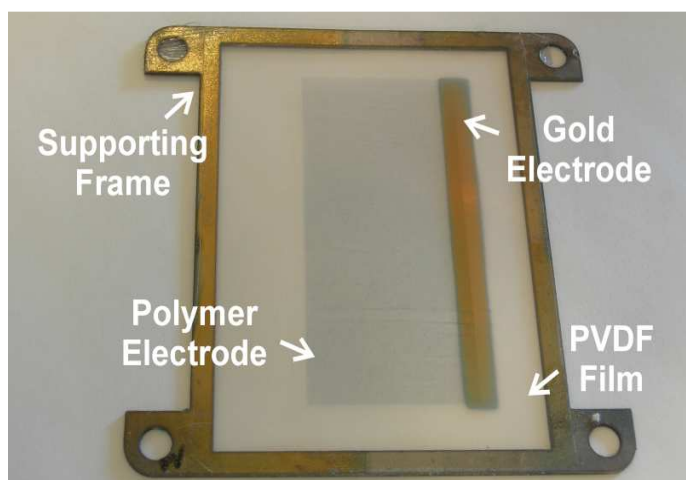


Figure 3.1 PVDF film tensioned on a supporting frame with CPS and gold electrodes.

Lamination

Figure 3.2 schematically shows laminated bilayers with electrodes on three and all four sides. Four sided samples work well if the lamination is poor with gaps or air pockets. For high quality laminations, however, three sided samples exhibit higher strain because there is less passive electrode material constraining motion. Three sided samples are also easier to fabricate, requiring one less electrode deposition step. Simultaneous external pressure and heat are applied to both films for successfully lamination. The layers are compressed using a vacuum bag (~ 10 cmHg) and then placed in an oven. The temperature (100°C) and heat exposure time (2 hours) are optimized to maximize the interlayer bounding strength and equalize the capacitance between the three and four layer designs. The optimized lamination process gave bilayers with similar average capacitance (251 nF for 3 sided samples and 268 nF for 4 sided samples, see Appendix B), indicating a high quality lamination. In theory, one could use only two electrodes in the bilayer if the final step in the vacuum oven provides a sufficiently high quality lamination of the rolled bilayer.

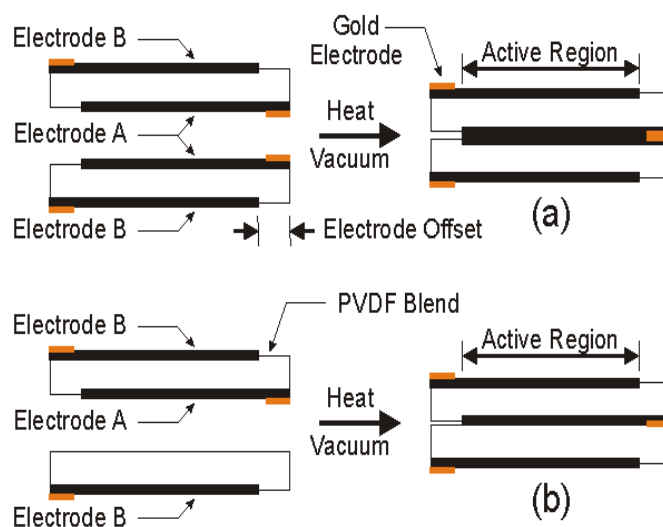


Figure 3.2 Bilayer lamination with electrodes on (a) 4 sides and (b) 3 sides.

Rolling

Rolling transforms the flat bilayer to a wound roll actuator. The bilayer is removed from the metal frame. Figure 3.3 shows the mandrel acting as a core to wind the film around. During winding, the bilayer is pulled along a flat surface by the rotating mandrel with a weight on the film providing tension to prevent the formation of wrinkles. The mandrel temporarily adheres to the film during rolling using an adhesive. At temperatures above 80°C the adhesive liquefies, allowing the core to be easily removed from the actuator after the lamination in a vacuum oven. To prevent unraveling, another adhesive is lightly deposited on the end of the rolled sample, permanently bonding the last two layers.

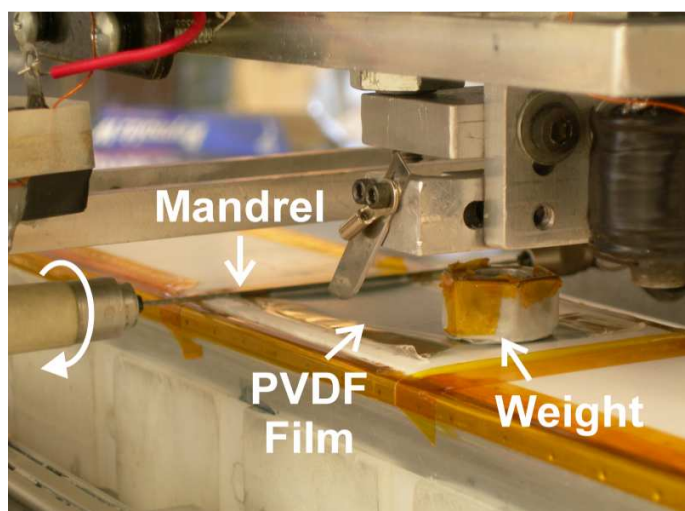


Figure 3.3 Automated mandrel for the rolling process.

Bonding and Electrical Contact

The last step of the actuator fabrication process is to heat the device at 90°C in a vacuum oven for 90 min. The vacuum helps eliminate air pockets trapped in between layers during the rolling process and the heat bonds all the rolled layers together, improving the mechanical strength of the structure. Removing residual air in the actuator is essential to improve the voltage breakdown of the device. Lastly, steel balls are bonded on both electrode ends using conductive epoxy to serve as electromechanical contacts (see Fig. 3.4).

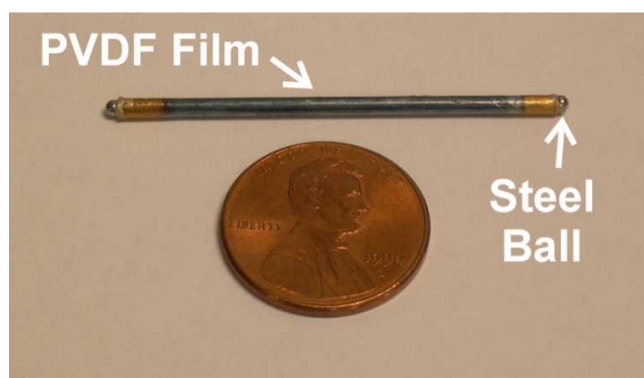


Figure 3.4 An example core-free rolled P(VDF-CFE-TrFE) actuator.

Chapter 4

Experiments

To characterize the properties of the actuators and confirm that they meet the Braille requirements, measurements of displacement, blocking force and capacitance are performed on several fabricated samples. The results are discussed in this section.

Experimental Set up

Figure 4.1 shows the experimental set up used to analyze the performance of 19 actuators fabricated using the process described in part III. A Trek 609E-6 high voltage amplifier, controlled by LabView, provides that actuation voltage. The displacement and blocking force are measured by a PolyTec OFV 534 laser vibrometer and a Transducer Techniques EBB-1 cantilever beam load cell, respectively. The current going through the actuator is also measured. An acrylic block is machined with 1.9 – 2.4 mm dia. holes to provide lateral support for the actuator. Golden fluid is pumped into the block to minimize arcing and improve heat dissipation. The steel balls of the actuator are contacted using a magnet on the bottom (positive end) that is fixed to the acrylic block and a magnet on the top that is soldered to a very thin (0.07 mm diameter) copper wire connected to ground.

Table 4.1 shows the average and standard deviation of the parameters and performance of the 19 actuators fabricated and tested. The devices average 2 mm in diameter and 43.6 mm in height formed from bilayers averaging 11 μm in thickness.

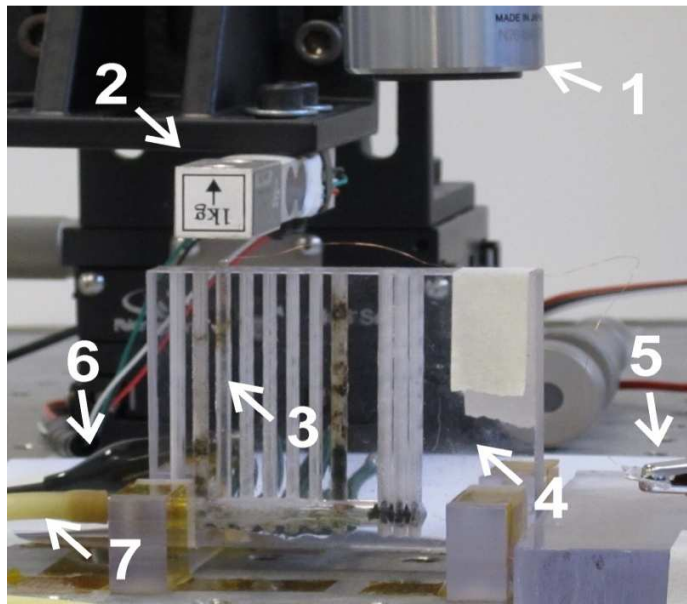


Figure 4.1 Displacement and force measurement set up. (1) Laser vibrometer. (2) Load cell. (3) Actuator. (4) Supporting acrylic block. (5) High voltage input. (6) Ground. (7) Golden fluid supply.

Table 4.1 P(VDF-TrFE-CFE) actuator properties

	Property	Average	Deviation	Max	Min
Geometrical	Length (mm)	43.6	1.2	45.4	42.0
	Active length (mm)	30	0	30	30
	Inner diameter (mm)	1.35	0.20	1.50	1.1
	Outer diameter (mm)	2.00	0.14	2.24	1.75
	Thickness of bilayer (μm)	11	2	16	7
Electrical	Capacitance @ 20 Hz (nF)	260	49	349	185
	Loss @ 20 Hz	0.08	0.02	0.14	0.04
Mechanical	Strain at 100 V/ μm (%)	2.03	0.81	4.18	0.82
	Force at 100 V/ μm (N)	1.05	0.26	1.30	0.70
	Stiffness at 50 V/ μm (kN/m)	4.15	1.16	6.04	2.77

Electrical Measurements

The capacitance and loss of the actuators are measured using a precision LCR meter (HP 4284A). The theoretical capacitance

$$C = \frac{\epsilon_0 \epsilon_r A}{t},$$

where ϵ_0 is the electric constant, ϵ_r is the relative permittivity of P(VDF-CFE-TrFE), A is the active area of the actuator, and t the thickness of the single layer film. For the average parameters in Table II and permittivity $\epsilon_r = 40$ the expected value of capacitance is 290 nF. The actual measured capacitance is less than theoretically predicted, probably due to incomplete electroding of the bilayer surfaces. The loss is also relatively high due to resistance in the CPS electrodes.

Strain Results

The voltage applied during initial strain testing ranged from 200 V to approximately 700 V in 50 V increments. Two of the nineteen actuators fabricated failed immediately at 200 V. Of the remaining 17 samples, 12 survived the entire experiment and the other 5 failed at various input voltages due to film defects (see Appendix C).

Fig. 4.2 shows the experimental results for an example device. The voltage signal is ramped at 100 V/s until reaching the desired value (Fig. 4.2(a)). The signal is held constant for 60 seconds before being ramped back down to zero. Using a ramp input rather than a step input limits the maximum current during the charging process to about 0.1 mA (Fig. 4.2(b)). A step input of 650 V generates a current peak of approximately 2 mA, more than an order of magnitude higher. High currents are likely to cause heating at localized imperfections that ultimately lead to breakdown. Figure 4.2(c) shows the displacement response of the actuator peaking at more than 1.2 mm for an applied voltage of 750 V. After a quick initial transient, the actuator continues to

slowly extend. This extension eventually reaches a constant steady state value after approximately 600 s. When the voltage is turned off, the actuator quickly contracts and then slowly returns to zero displacement. This ‘reversible creep effect’²⁰ has been observed in piezoelectric materials.

Figure 4.3 shows the average and standard deviation of strain versus electric field for the 17 actuators tested (the results at 100 MV/m are also in Tab. II). At 100 MV/m, the average strain is 2%, much lower than the performance expected from previously tested single layer P(VDF-CFE-TrFE) films¹⁴. The standard deviation is relatively large at medium and high strains. This variability can be explained by several factors. First, the actuators tend to move axially *and transversely*. The acrylic block constrains this transverse movement but does not entirely eliminate the associated reduction in the desired axial displacement. Second, the capacitance data also shows significant uncertainty, indicating variances in material properties and uniformity of the electrode deposition. On average, actuators with higher capacitance also produce higher displacement. Third, the adhesive deposited during the rolling process, although minimal, could restrain the axial displacement.

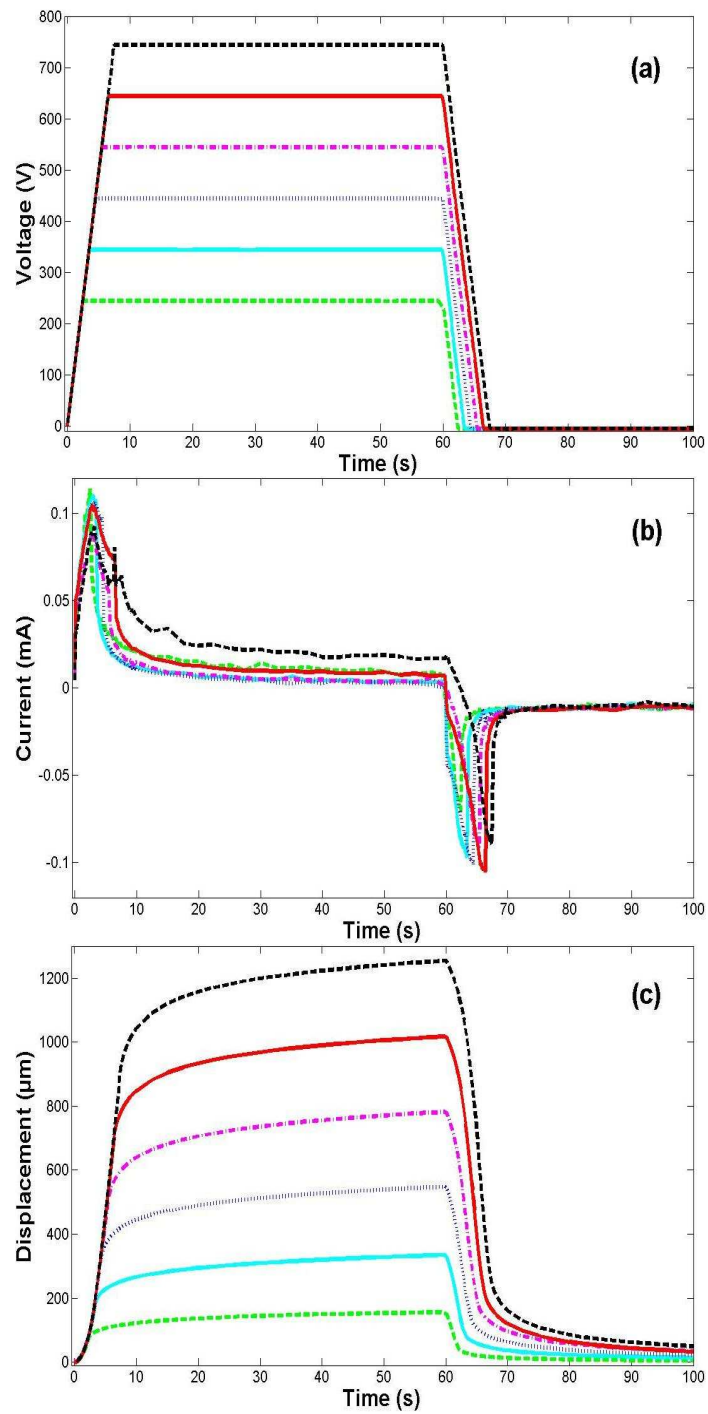


Figure 4.2 Experimental time response for an example actuator: (a) Voltage, (b) Current, and (c) Displacement.

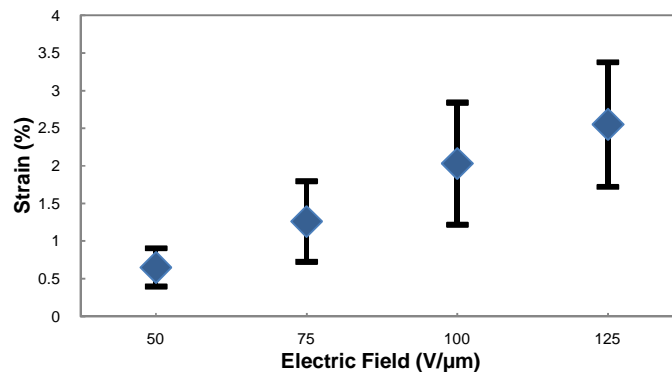


Figure 4.3 Experimentally measured strain versus electric field for 17 actuators (blue diamond is the mean value and error bars indicate \pm one standard deviation).

Force Results

Eight actuators are successfully tested for blocking force by positioning the actuator tip in contact with the load cell and applying the voltage time trajectory shown in Fig. 4.4(a). The voltage is ramped up, held constant for 30 s and ramped down. The blocking force results for one actuator are shown in Fig. 4.4(b). For most of the actuators, the response looks similar to this example for voltages less than 300 V (see Appendix D). The blocking force rises until the applied voltage ramps down. The blocking force at that voltage is chosen to be the value just before the down ramp starts. For the example actuator at 400 V, however, the blocking force does not grow monotonically, peaking before the downward ramp. In this case, the blocking force produced by the device is higher than the critical Euler load of the structure and the tube bends laterally. The side walls of the acrylic block limit buckling to a certain extent but at 700 V the actuator fails and no longer withstands high loads.

Fig. 4.5 shows the average force and standard deviation for all tested samples with summary results in Table II. On average, the actuators are capable of producing 1 N of force at 100 MV/m. Buckling typically first occurs at electric fields near 85 MV/m and failure is most likely around 125 MV/m. This behavior is predicted by the buckling analysis in Section II,

although the expected blocking force and buckling load are roughly ten times larger than the experimental measurements. Weak bonding between the layers and geometric imperfections in the fabricated actuators may be responsible for the reduced experimentally observed buckling load. The lower forces overall may be due to unmodeled softness in the load path or lower material stiffness caused by high temperature processing during lamination.

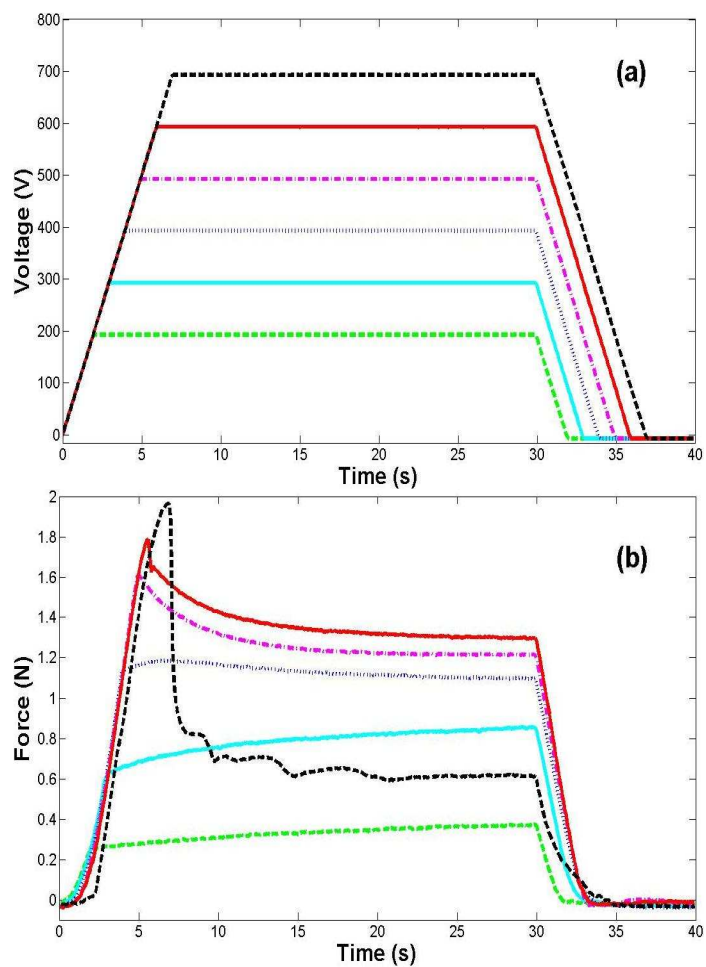


Figure 4.4 Experimental time response for blocking force tests: (a) Voltage and (b) Blocking force.

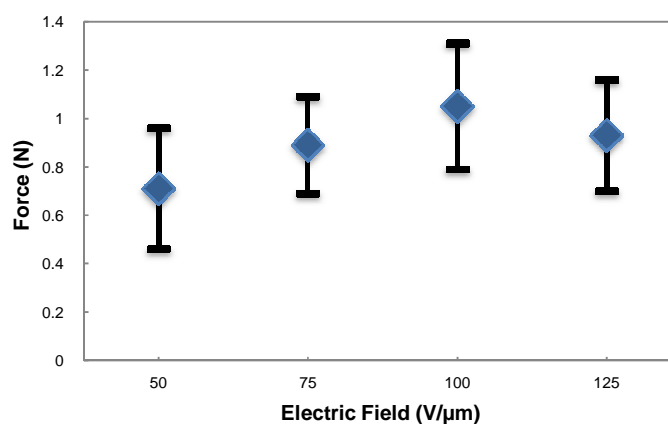


Figure 4.5 Average blocking force versus electric field for 8 actuators (blue diamond is the mean value and error bars indicate \pm one standard deviation).

Self Healing

Electrical breakdown is a major concern in the design of the actuator and several failed due to high current and/or voltage operation. The film can have small pin holes (diameter of a few microns) and, as shown in Fig. 4.6, electrode deposition can connect the positive and negative electrodes of the actuator. This shorts the device and could cause complete failure of the actuator even at low electric fields. The CPS electrode and the PVDF blends used in this actuator, however, exhibit a self-healing effect. It is believed that short burns locally and isolates the defect from the remainder of the electrode. The electrodes disconnect are no longer shorted and the actuator can function as planned. Figure 4.7 shows the voltage, current, and displacement of an actuator during a self-healing event. At $t = 5.5\text{s}$, the current exhibits a sudden peak, corresponding to the burning of a defect. Simultaneously, the actuation of the device is temporarily reduced but quickly recovers its previous trend.

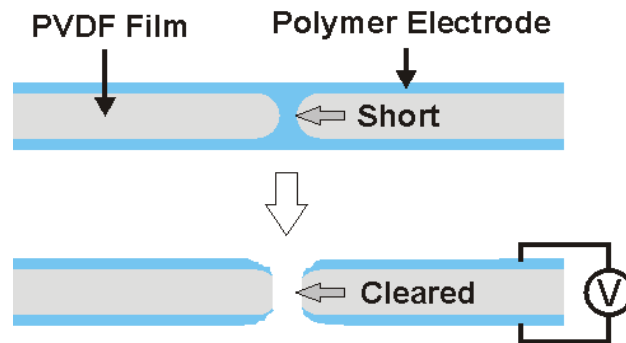


Figure 4.6 Self-healing effect in PVDF terpolymer.

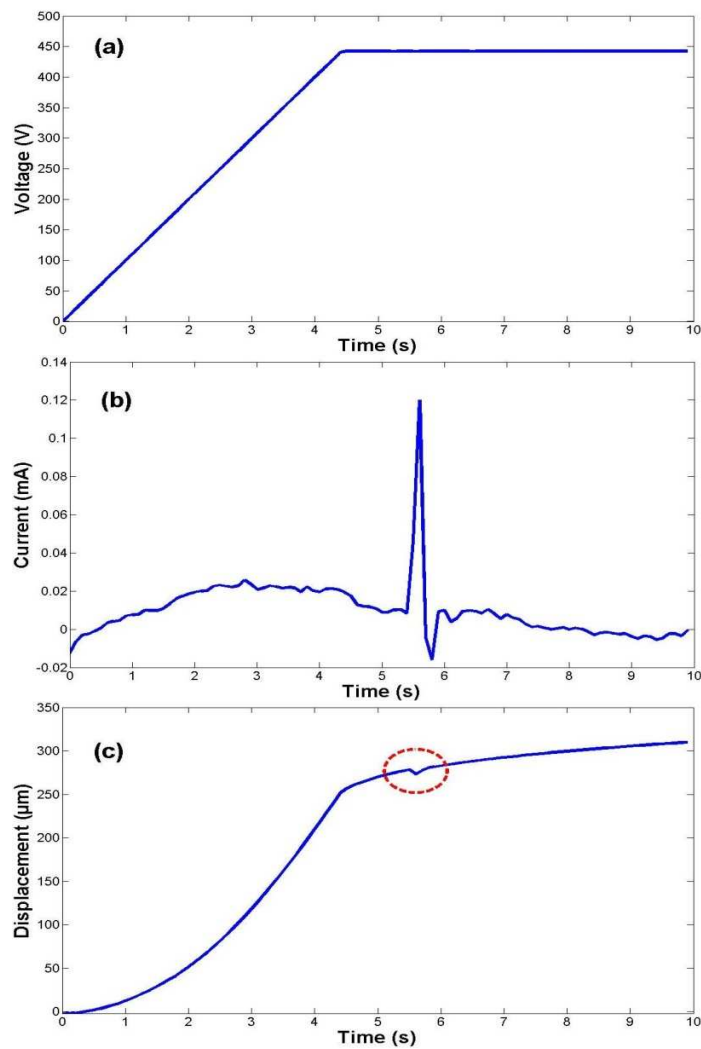


Figure 4.7 Experimental self-healing event time response: (a) Voltage, (b) Current, and (c) Displacement.

Frequency Response and Cycle Life

Frequency response and cycle life of the device are still in the testing phase, as more samples are needed to get sufficient data (see Appendix E). The actuators have a much lower reliability when used in AC as compared to DC. At frequencies above 10Hz, they tend to break down and burn within a few cycles, even at low voltages. It is believed that heat accumulation due to higher currents is causing this failure. One actuator survived 1000 cycles at 0.2 Hz and 700 V.

Chapter 5

Braille Cell Design

In this section, we present the Braille application the actuators were originally designed for. Figure 5.1 shows a Braille cell using six actuators that is designed, fabricated, and tested.

The cell dimensions are 40 mm × 12 mm × 70 mm. It is composed of three subparts:

- A top section, which contains the ceramic pins that the user touches. The pins are 2.5 mm apart, and are connected to a metal plate that acts as a common ground. A magnet is glued on the bottom of each pin to contact the actuators.
- A central acrylic block, which is the housing for the actuators. Six holes of 2.2 mm diameter are drilled 2.5 mm apart. A separate hole is used to pass a ground wire to the top metal plate.
- A plastic base containing six set screws that contact the positive end of the actuators. Each screw can be used to compensate for differences in the initial lengths and displacement performance of the actuators.

The cell is integrated into a demonstration box, containing all the necessary electronics and batteries to activate the actuators at 550 V. A ribbon cable plugs into the bottom of the cell, connecting to the set screws and to the ground wire. Each pin can be individually turned on or off using switches mounted on the box. The device is currently being tested by the blind community.

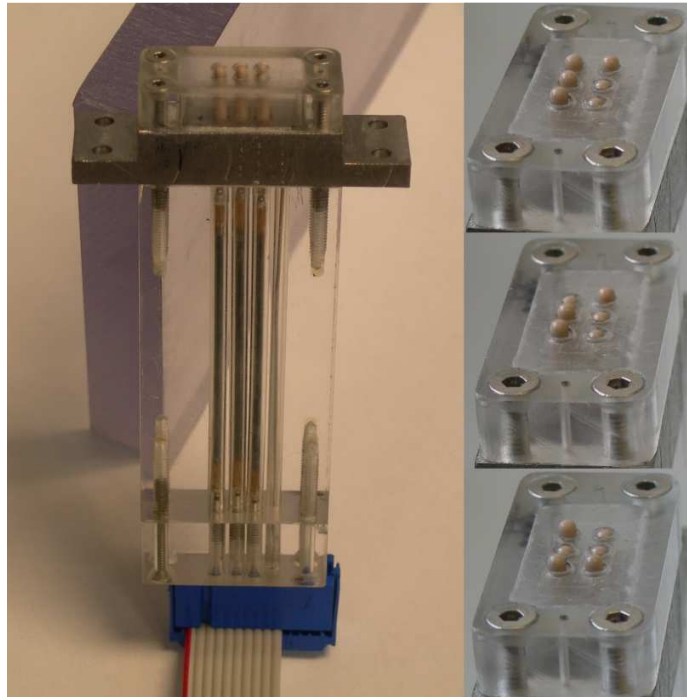


Figure 5.1 Picture of the Braille cell with close-up views of the six pins spelling 'PSU'.

Chapter 6

Conclusion and Future Work

A core-free P(VDF-CFE-TrFE) thin film rolled actuator can be fabricated using solution casting, stretching/annealing, electroding, laminating, rolling, bonding, and electrical contacting. The size of the actuator is scalable based on the width and length of available films and the number of layers. In this research, 2 mm diameter and 44 mm long actuators are fabricated and shown to provide up to 4% strain and 1 N of blocking force at 100 MV/m. The actuators display beneficial self-healing and detrimental reversible creep. To prevent premature failure, the current (and hence bandwidth) of the actuators must be limited. A Braille cell using a 3×2 array of these actuators is successfully demonstrated. The actuators may also be suitable for a wide range of other applications, including artificial muscles, mechanisms, smart structures, and robotics.

In the future, the biggest challenge will be to fully automate the fabrication process of the actuator, replacing the supporting frames by manufacturing machines capable of performing electrode deposition, lamination and rolling from rolls of P(VDF-CFE-TrFE). This would considerably reduce the production time of the actuators as well as cost and workforce, and is necessary if this technology is to be implemented in full page Braille displays that require thousands of actuators.

Concerning the design of the device itself, several changes could be made to improve performance and handiness. Using other electrodes than CPS could improve the electromechanical response of the actuators. Currently, aluminum electrodes are being tested as a new alternative. Modifying the electrode pattern such that both positive and negative contacts are on the same end of the device would also make electrical connections easier.

Finally, more experiments need to be conducted to better understand the characteristics of the actuator and the PVDF blends themselves. Looking at frequency response, as well as reliability, would help understand why those devices work well in DC, but fail after a few AC cycles.

Understanding and modeling the physical phenomenon behind the slow reversible creep effect of the displacement response would be a major advancement in the characterization of this material.

References

- [1] Y. Bar-Cohen, "Refreshable Braille displays using EAP actuators", *Proc. of SPIE*, vol. 7642, 764206, 2010.
- [2] G. Kovacs, L. Düring, "Contractive tension force stack actuator based on soft dielectric EAP", *Proc. of SPIE*, vol. 7287, 72870A, 2009.
- [3] M. Matysek, P. Lotz, H. F. Schlaak, "Tactile display with dielectric multilayer elastomer actuators", *Proc. of SPIE*, vol. 7287, 72871D, 2009.
- [4] Z. Yu, X. Niu, P. Bochu, W. Yuan, H. Li, B. Chen, Q. Pei, "Bistable electroactive polymers (BSEP) : large-strain actuation of rigid polymers", *Proc. of SPIE*, vol. 7642, 76420C, 2010.
- [5] H. R. Choi, D. Kim, N. H. Chuc, N. H. Lam Vuong, J. Koo, J. Nam, Y. Lee, "Development of integrated tactile display devices", *Proc. of SPIE*, vol. 7287, 72871C, 2009.
- [6] F. Carpi, G. Frediani, D. De Rossi, "Hydrostatically coupled dielectric elastomer actuators for tactile displays and cutaneous stimulators", *Proc. of SPIE*, vol. 7642, 76420E, 2010.
- [7] N. Di Spigna, P. Chakraborti, D. Winick, P. Yang, T. Ghosh, P. Franzon, "The integration of novel EAP-based Braille or cells fuse in a refreshable tactile display", *Proc. of SPIE*, vol. 7642, 76420A, 2010.
- [8] Q.M. Zhang, V. Bharti Zhao, "Giant electrostrictive response and ferroelectric relaxor behavior in electron irradiated polyvinylidene fluoride-trifluoroethylene polymer", *Science*, 280, 2101 (1998).

- [9] F. Xia, Z. Y. Cheng, H. S. Xu, Q. M. Zhang, G. Kavarnos, R. Ting, G. Abdul-Sedat, K. D. Belfield, "High electromechanical responses in terpolymer of P(VDF-TrFE-CFE)", *Adv. Mater.* 14, 1574 (2002).
- [10] Q.M. Zhang, C. Huang, F. Xia, J. Su, in: Y. Bar-Cohen (Ed.), *Electroactive Polymer Actuators as Artificial Muscles*", SPIE Optical Engineering Press, WA, 2004, Chapter 4.
- [11] N. H. Chuc, J. Koo, Y. Lee, J. Nam, H. R. Choi, "Artificial muscle actuator based on the synthetic elastomer", *International Journal of Control, Automation and Systems*, vol. 6, no. 6, pp. 894-903, 2008.
- [12] Q. Pei, M. Rosenthal, R. Pelrine, S. Stanford, R. Kornbluh, "Multifunctional elastomer roll actuators and their application for biomimetic walking robots", *Proc. of SPIE*, vol. 5051, pp. 281-290, 2003.
- [13] A. Rajamani, M. D. Grissom, C. D. Rahn, Q. Zhang, "Wound roll dielectric elastomer actuators : fabrication, analysis, and experiments", *IEEE/ASME Transactions on Mechatronics*, vol. 13, no. 1, pp. 117-124, 2008.
- [14] M. Tryson, H. E. Kiil, M. Benslimane, "Powerful tubular core free dielectric electro active polymer (DEAP) 'PUSH' actuator", *Proc. of SPIE*, vol. 7287, 72871F, 2009.
- [15] G. Kovacs, S. M. Ha, S. Michel, R. Pelrine, Q. Pei, "Study on core free rolled actuators based on soft dielectric EAP", *Proc. of SPIE*, vol. 6927, 69270X, 2008.
- [16] K. Ren, S. Liu, M. Lin, Y. Wang, Q. M. Zhang, "A compact electroactive polymer actuator suitable for refreshable Braille display", *Sensors and Actuators A: Physical*, vol. 143, issue 2, pp. 335-342, 2007.
- [17] K. Ren, S. Liu, M. Lin, Y. Wang, Q. M. Zhang, "Ferroelectric relaxor polymers as intelligent soft actuators and artificial muscles", in *Intelligent materials*, book auth. M. Shahinpoor, H. J. Sneider, 2008.

- [18] National Library Service for the Blind and Physically Handicapped, “Braille Books and Pamphlets”, *Library of Congress*, Sec. 3.2 in Spec. 800, 2008.
- [19] S.Timoshenko, J. Gere, *Theory of Elastic Stability*, 2nd Ed., New York: McGraw-Hill, 1961, pp. 49-50.
- [20] R. Jones, J. Oubaek, R. Sarban, “Creep effect modeling for a core-free tubular actuator”, *Proc. of SPIE*, vol. 7287, 728769, 2009.

Appendix A

Capacitance and Loss data of the PVDF single layers

Table A.1 Electrode spraying data for single layers of P(VDF-TrFE-CFE) blends.

Sample Thickness (μm)	Volume sprayed (mL)	C @ 20 Hz (nF)	C @ 100 Hz (nF)	C @ 1000 Hz (nF)	Loss @ 20 Hz	Loss @ 100 Hz	Loss @ 1000 Hz
6.5	750	126	115	37	0.1	0.21	1.28
4.5	750	41	39	28	0.1	0.11	0.53
5	750	108	96	39	0.12	0.22	1.01
4	1000	128	119	92	0.13	0.11	0.44
4	1000	134	126	98	0.12	0.11	0.41
4	1000	165	156	126	0.1	0.09	0.4
5	1000	59	55	37	0.11	0.12	0.59
5	1000	183	172	144	0.11	0.09	0.32
5	1000	102	95	70	0.09	0.11	0.46
5	1000	167	158	136	0.08	0.08	0.28
5.5	1000	171	162	141	0.14	0.09	0.28
8	1000	93	86	77	0.14	0.09	0.17
6.5	1000	66	58	21	0.17	0.25	1.11
5.5	1000	79	74	63	0.11	0.09	0.27
7	1250	135	126	109	0.12	0.09	0.27
8	1250	122	113	98.5	0.14	0.1	0.26
4	1250	177	166	144	0.11	0.09	0.27
4.5	1250	174	164	146	0.1	0.08	0.22
5	1250	169	160	146	0.1	0.07	0.17
4.5	1250	220	207	172	0.09	0.09	0.35
5	1250	182	172	155	0.1	0.07	0.18
5	1250	79	73	54	0.1	0.11	0.38
8	1250	104	96	87	0.14	0.08	0.15
6	1500	143	133	120	0.11	0.08	0.14
6	1500	105	97	83	0.12	0.1	0.28
5	1500	130	121	109	0.1	0.08	0.18

Appendix B

Capacitance and Loss data of the PVDF bilayers

Table B.1 Electrode spraying data for bilayers of P(VDF-TrFE-CFE) blends.

Number sprayed sides	Sprayed amount (μL)	C @ 20 Hz (nF)	C @ 100 Hz (nF)	C @ 1000 Hz (nF)	Loss @ 20 Hz	Loss @ 100 Hz	Loss @ 1000 Hz
3	750	256	236	98	0.1	0.17	1.1
3	750	213	203	139	0.08	0.11	0.59
3	1000	284	268	176	0.09	0.11	0.64
3	1000	304	284	201	0.11	0.12	0.54
3	1000	111	106	73	0.11	0.12	0.6
3	1000	206	194	163	0.1	0.09	0.34
3	1250	259	248	220	0.06	0.07	0.27
3	1250	317	296	236	0.1	0.1	0.41
3	1250	208	193	173	0.14	0.09	0.19
3	1500	209	200	185	0.06	0.05	0.17
4	750	185	167	95	0.1	0.19	0.67
4	1000	292	277	236	0.08	0.08	0.33
4	1000	274	259	209	0.09	0.09	0.4
4	1000	349	334	276	0.06	0.08	0.39
4	1000	203	192	168	0.09	0.08	0.26
4	1250	254	244	224	0.07	0.06	0.18
4	1250	333	319	291	0.06	0.06	0.2
4	1250	282	272	248	0.04	0.05	0.2
4	1500	255	243	216	0.07	0.07	0.25

Appendix C

Displacement data of the PVDF actuators

In this section, we provide all the displacement measurements recorded for the 17 actuators that withstood at least 500 V input (Fig. A.1 to Fig. A.17). Each figure shows the applied voltage, the current flowing through the device, and the displacement response, all as a function of time. The input voltage was ramped at a rate of 100 V/s until reaching the desired value, to reduce the maximum current and avoid breakdown. A filter was used to remove the noise from the current signal, except for actuators number 5 and 8, which were tested before the filter was implemented. Finally, Fig. C.18 shows the strain vs. electric field for all samples, obtained by combining the displacement data, the applied voltage, and the bilayer thickness.

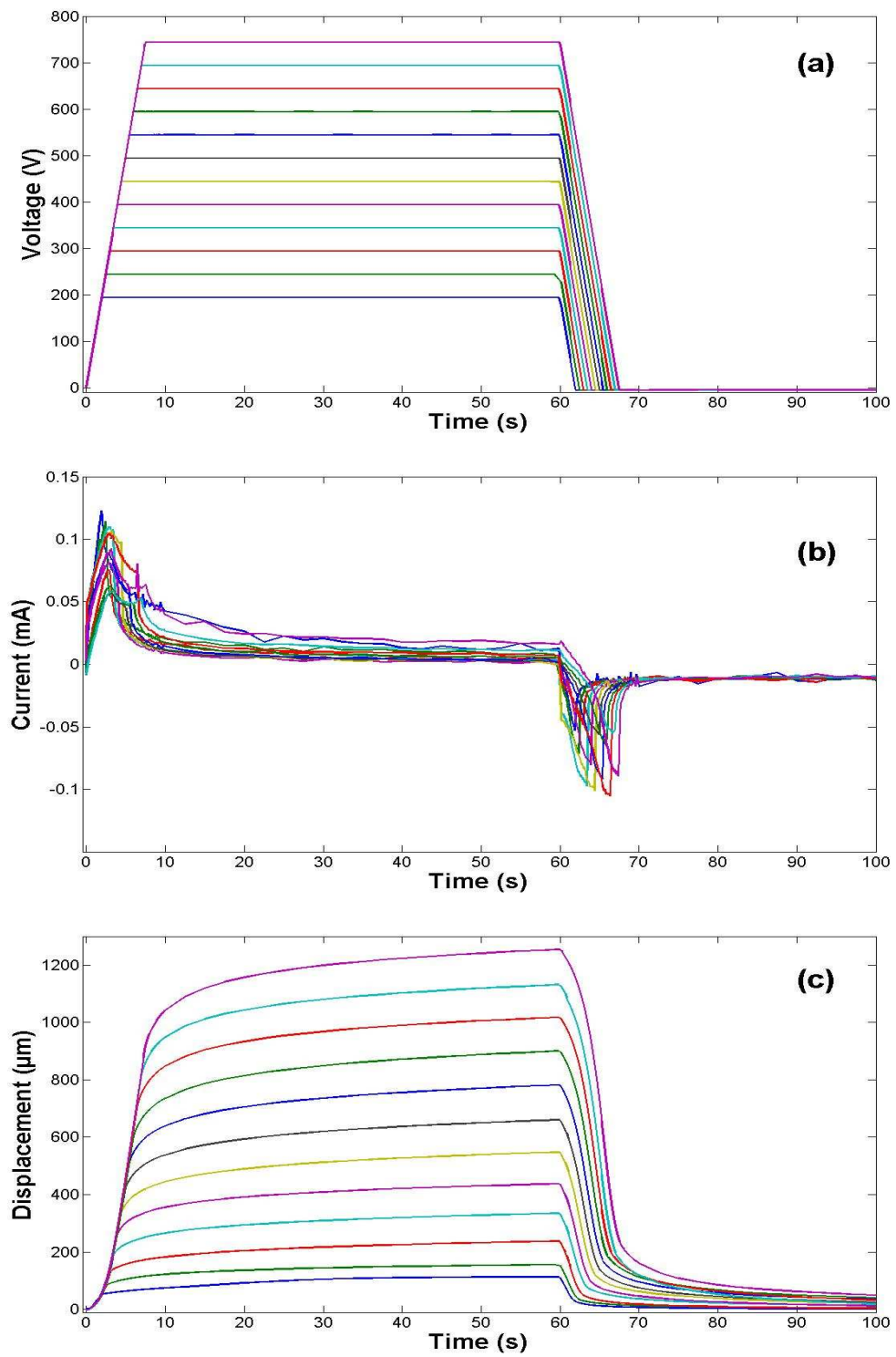


Figure C.1 Displacement characteristics of actuator #1 for voltages ranging from 200V to 750V. (a) Voltage vs. time. (b) Current vs. time. (c) Displacement vs. time.

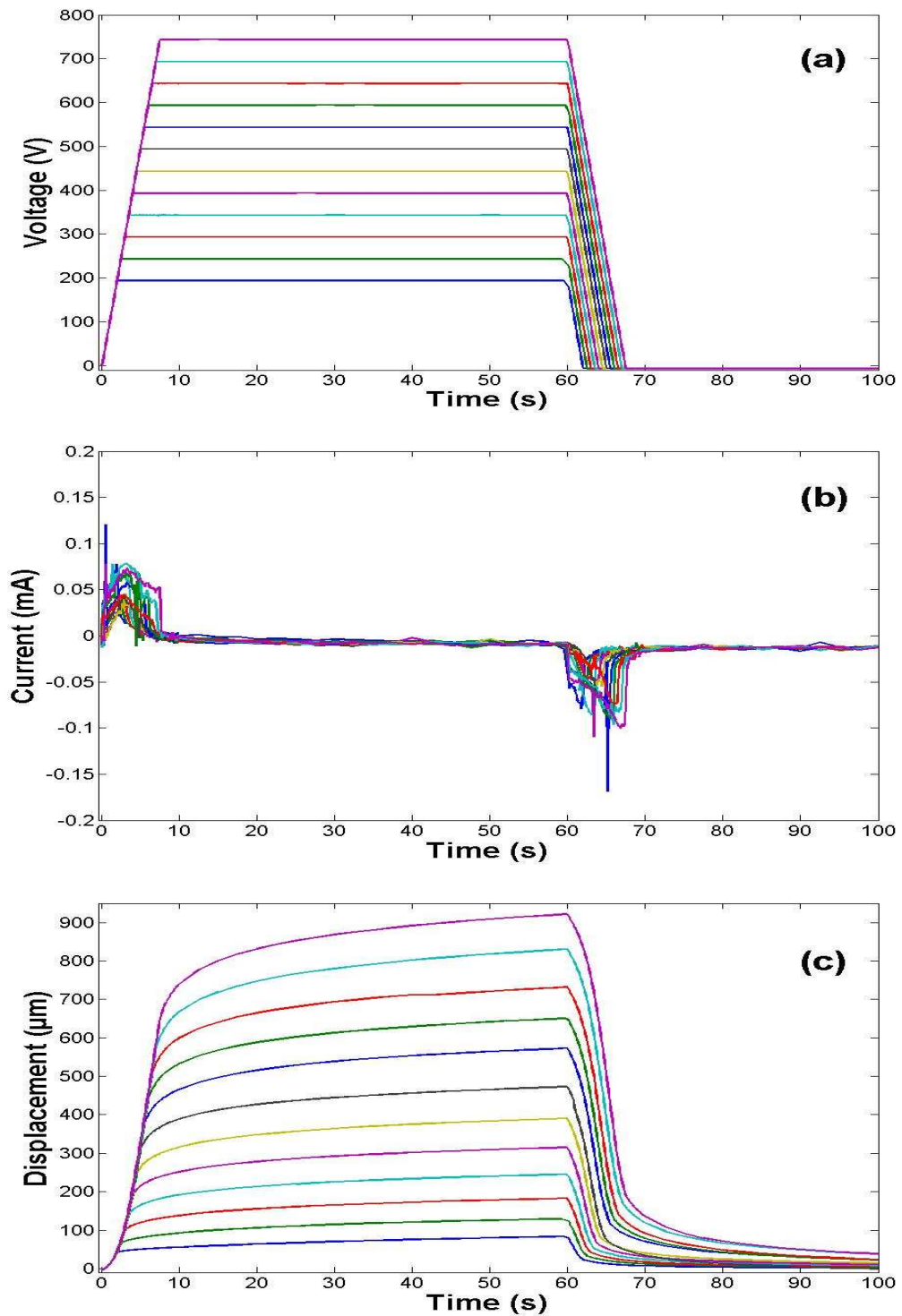


Figure C.2 Displacement characteristics of actuator #2 for voltages ranging from 200V to 750V. (a) Voltage vs. time. (b) Current vs. time. (c) Displacement vs. time.

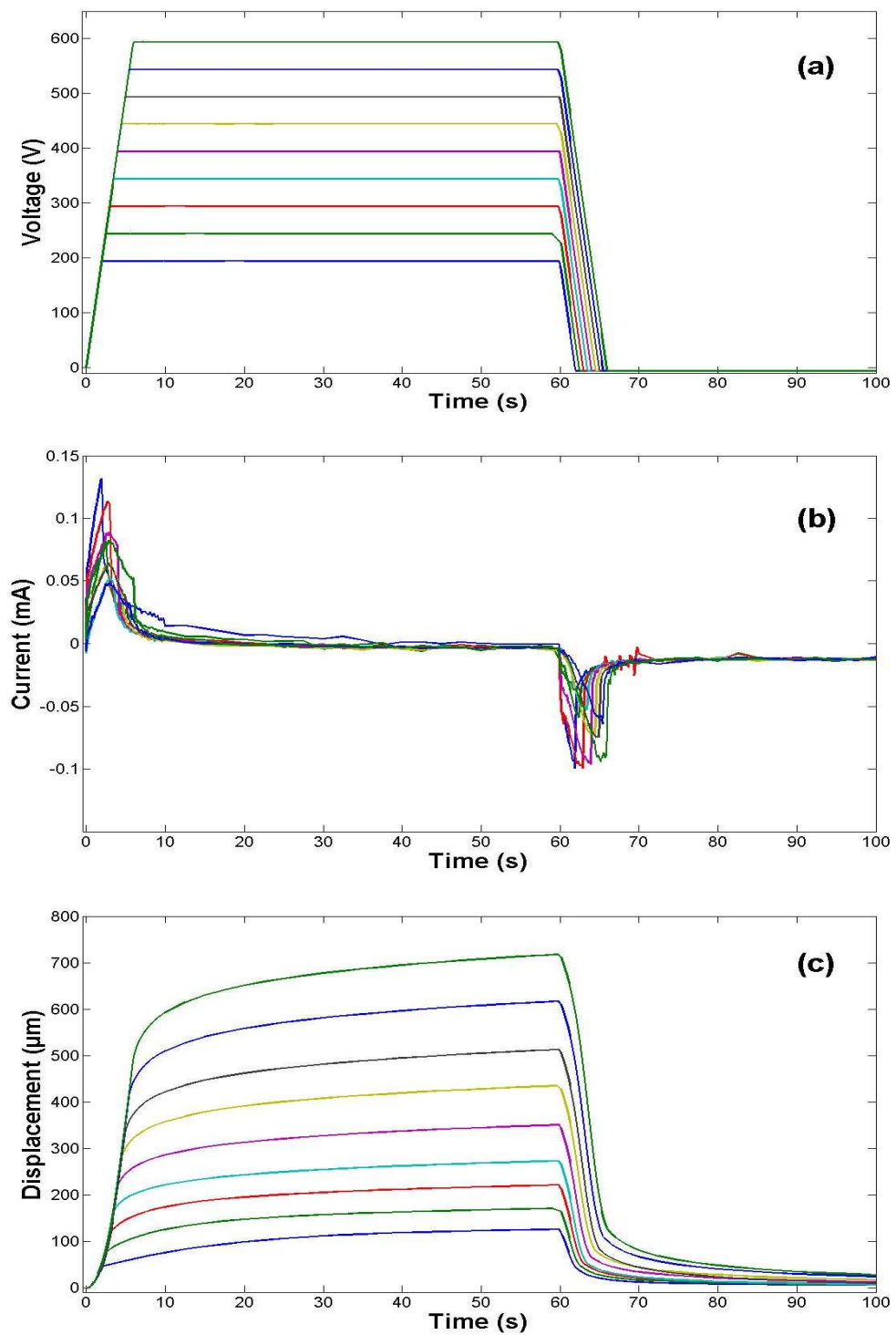


Figure C.3 Displacement characteristics of actuator #3 for voltages ranging from 200V to 600V. (a) Voltage vs. time. (b) Current vs. time. (c) Displacement vs. time.

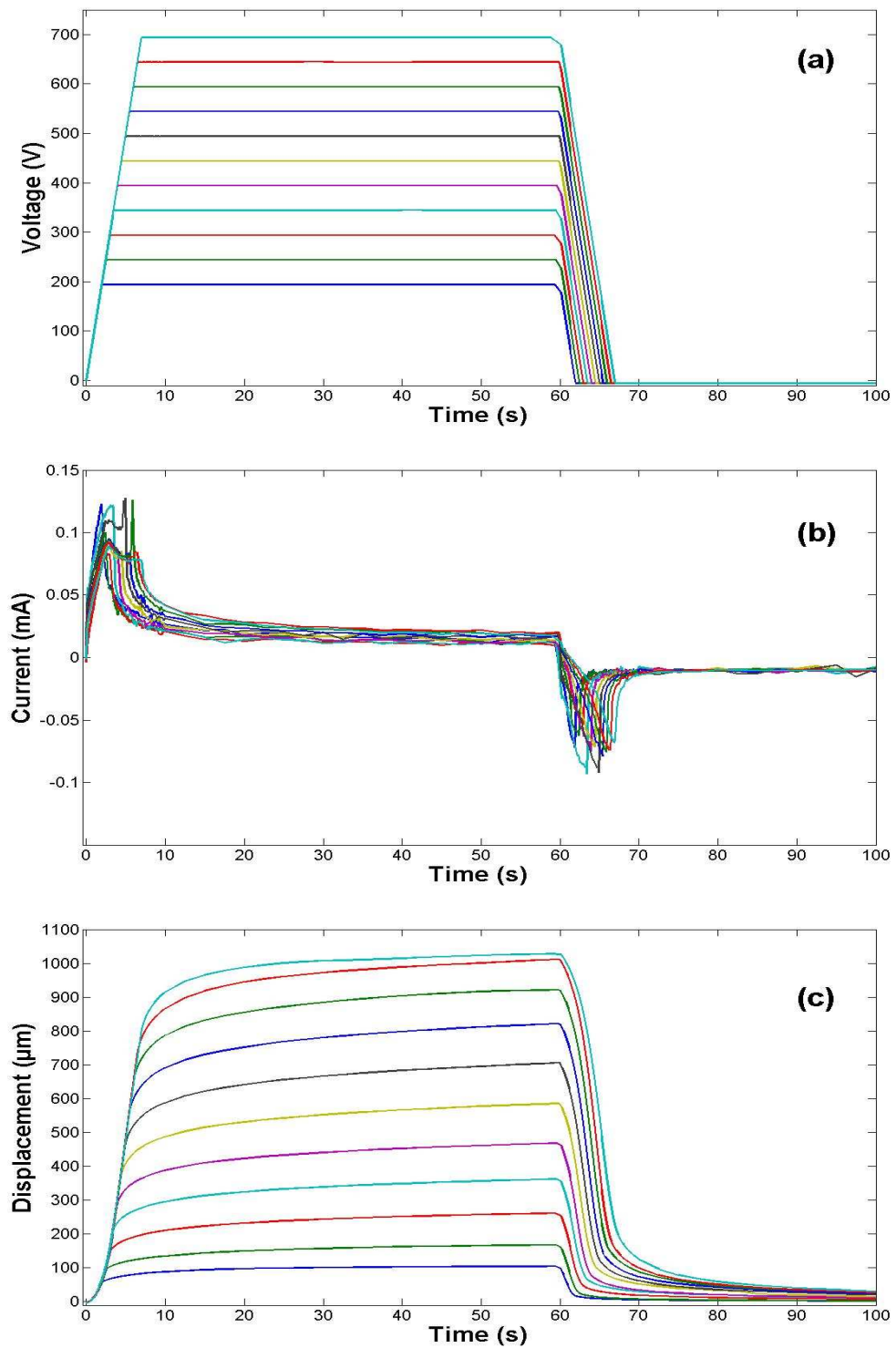


Figure C.4 Displacement characteristics of actuator #4 for voltages ranging from 200V to 700V. (a) Voltage vs. time. (b) Current vs. time. (c) Displacement vs. time.

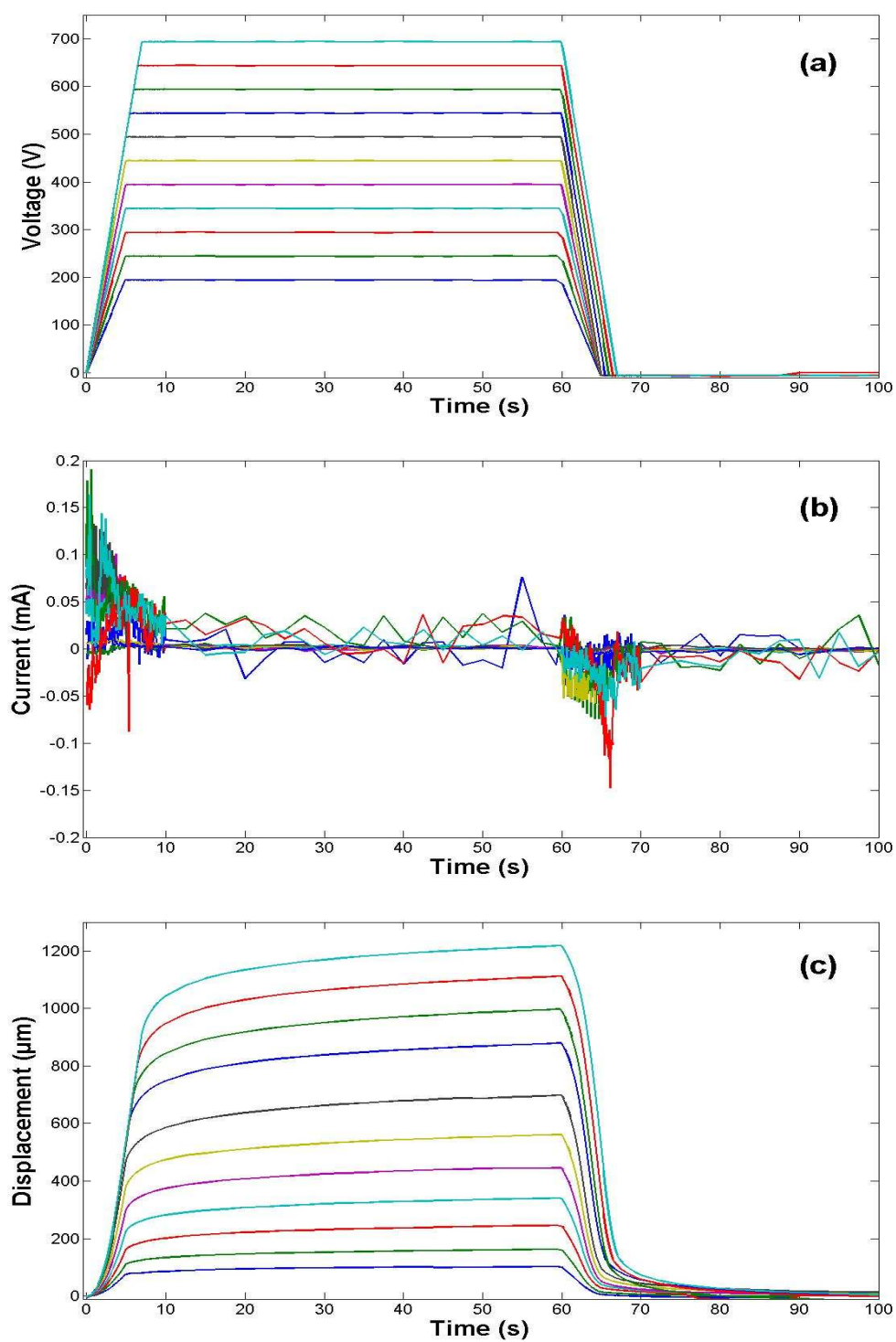


Figure C.5 Displacement characteristics of actuator #5 for voltages ranging from 200V to 700V. (a) Voltage vs. time. (b) Current vs. time. (c) Displacement vs. time.

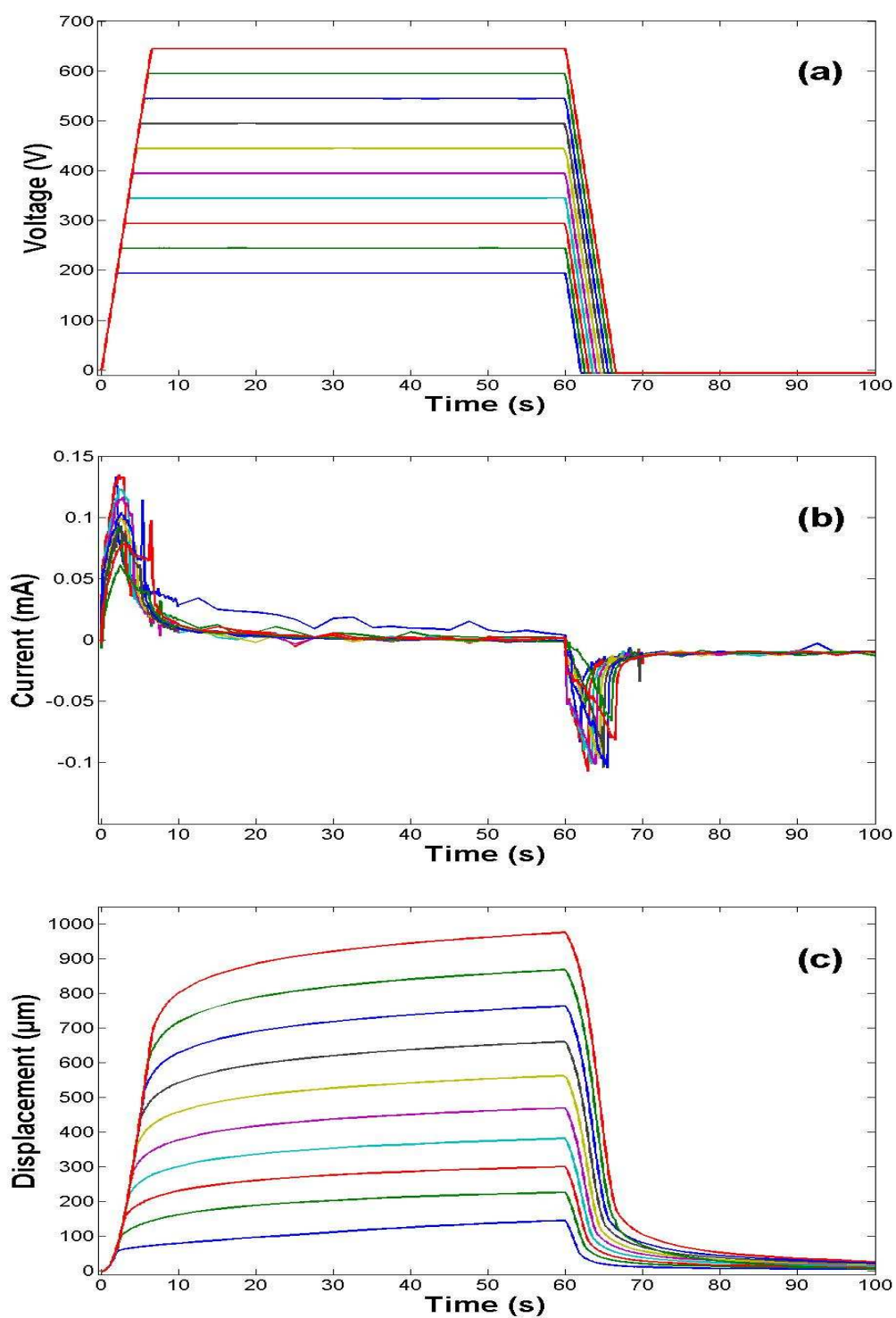


Figure C.6 Displacement characteristics of actuator #6 for voltages ranging from 200V to 650V. (a) Voltage vs. time. (b) Current vs. time. (c) Displacement vs. time.

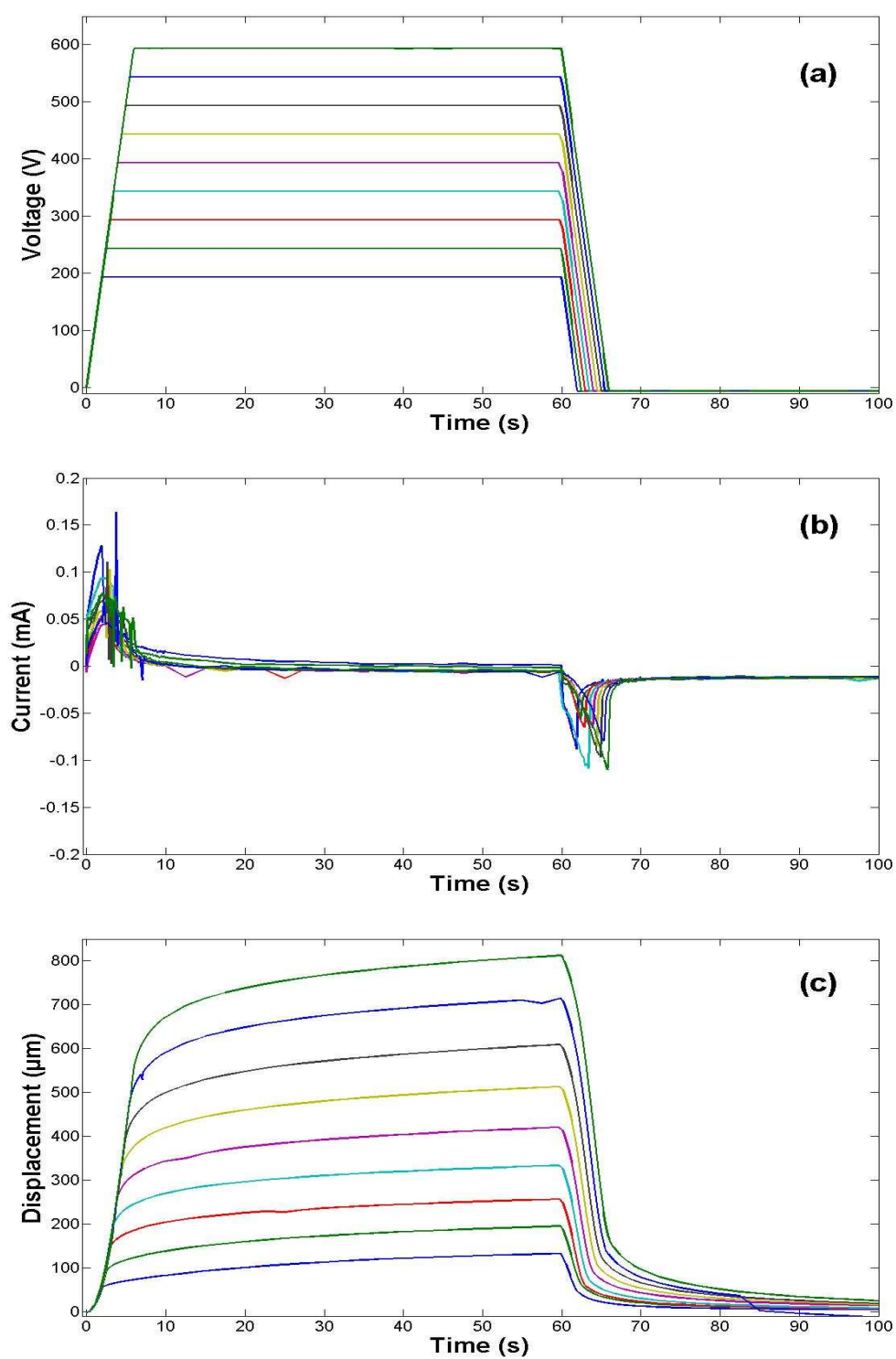


Figure C.7 Displacement characteristics of actuator #7 for voltages ranging from 200V to 600V. (a) Voltage vs. time. (b) Current vs. time. (c) Displacement vs. time.

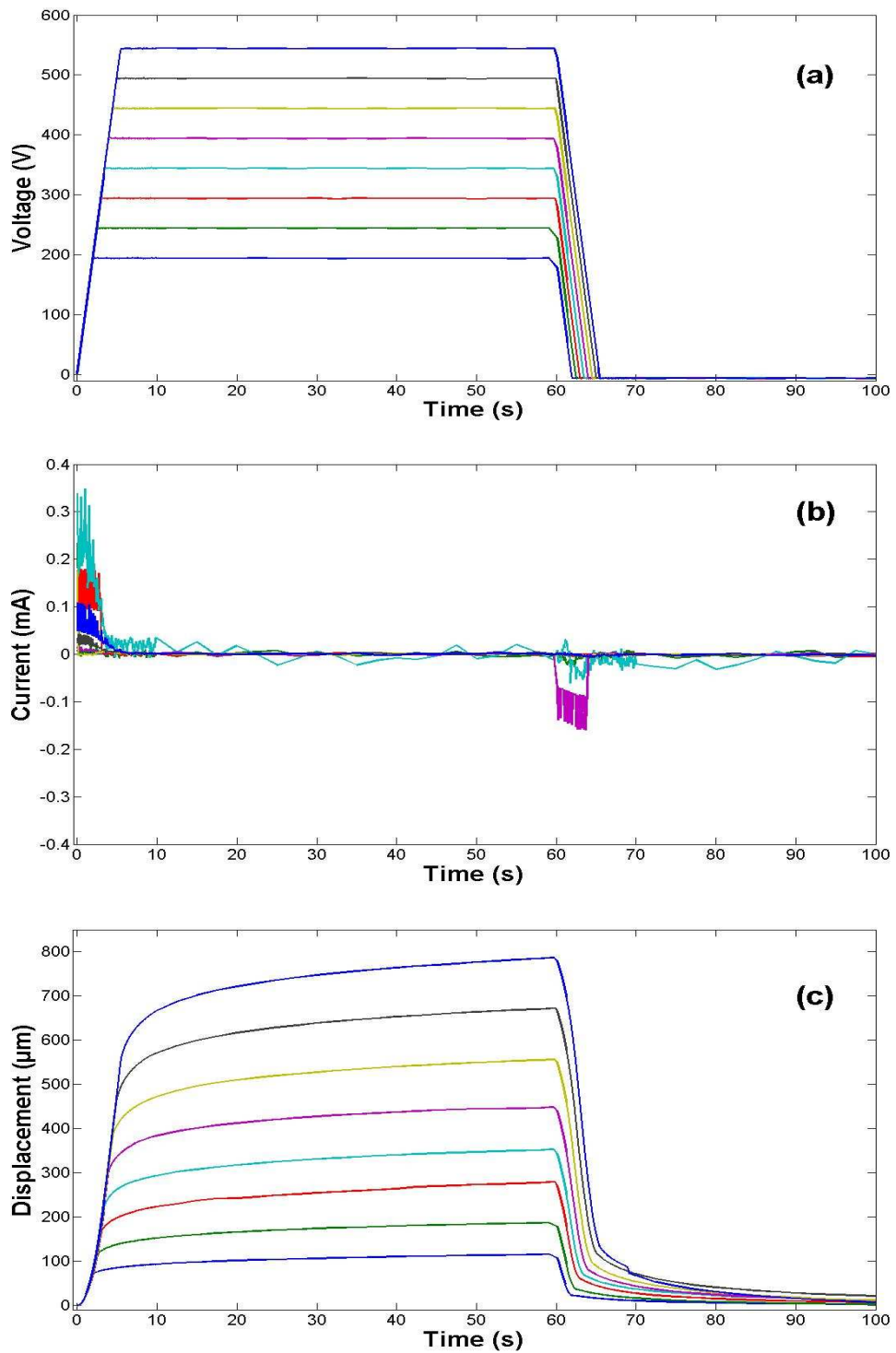


Figure C.8 Displacement characteristics of actuator #8 for voltages ranging from 200V to 550V. (a) Voltage vs. time. (b) Current vs. time. (c) Displacement vs. time.

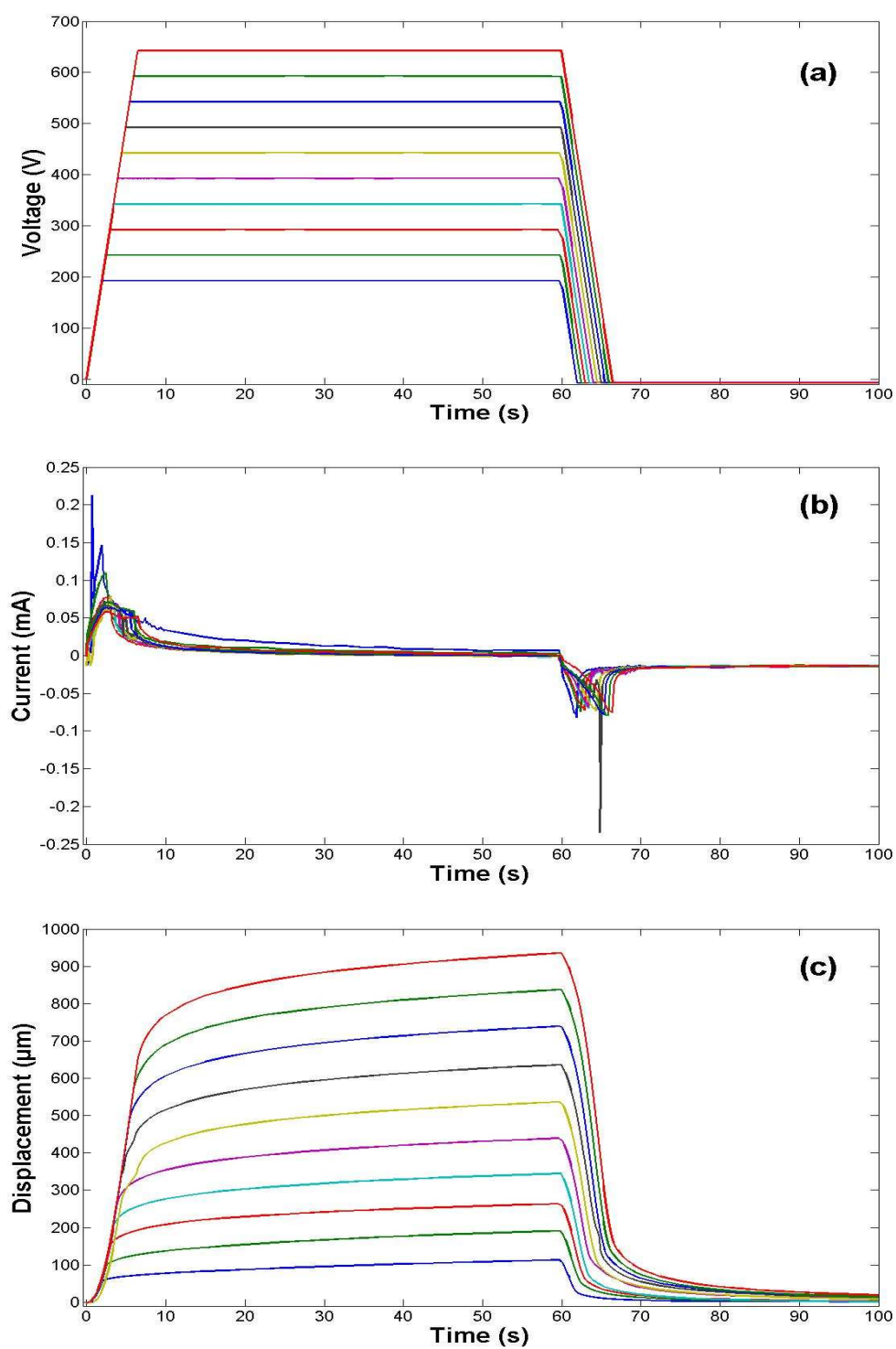


Figure C.9 Displacement characteristics of actuator #9 for voltages ranging from 200V to 650V. (a) Voltage vs. time. (b) Current vs. time. (c) Displacement vs. time.

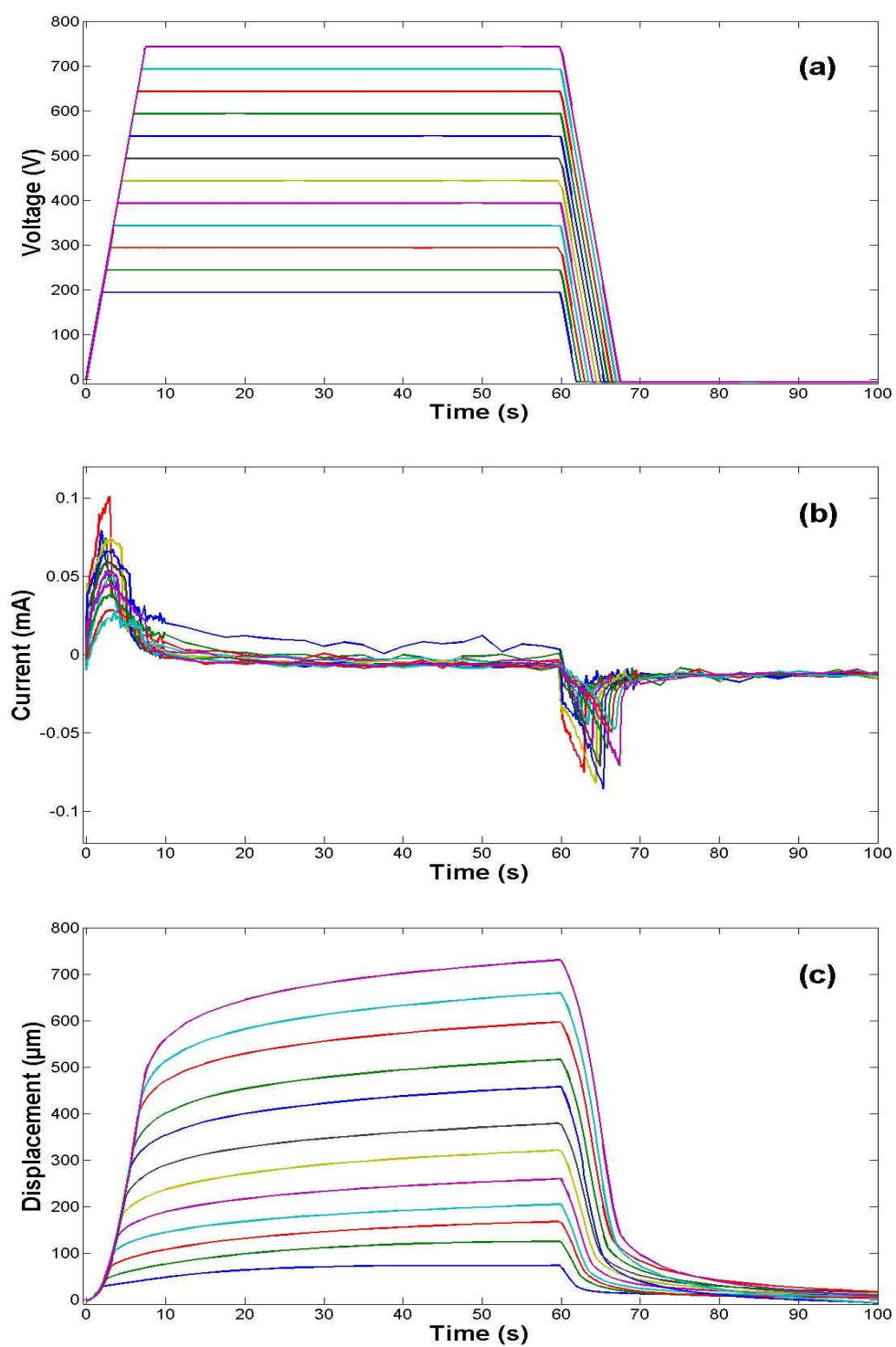


Figure C.10 Displacement characteristics of actuator #10 for voltages ranging from 200V to 750V. (a) Voltage vs. time. (b) Current vs. time. (c) Displacement vs. time.

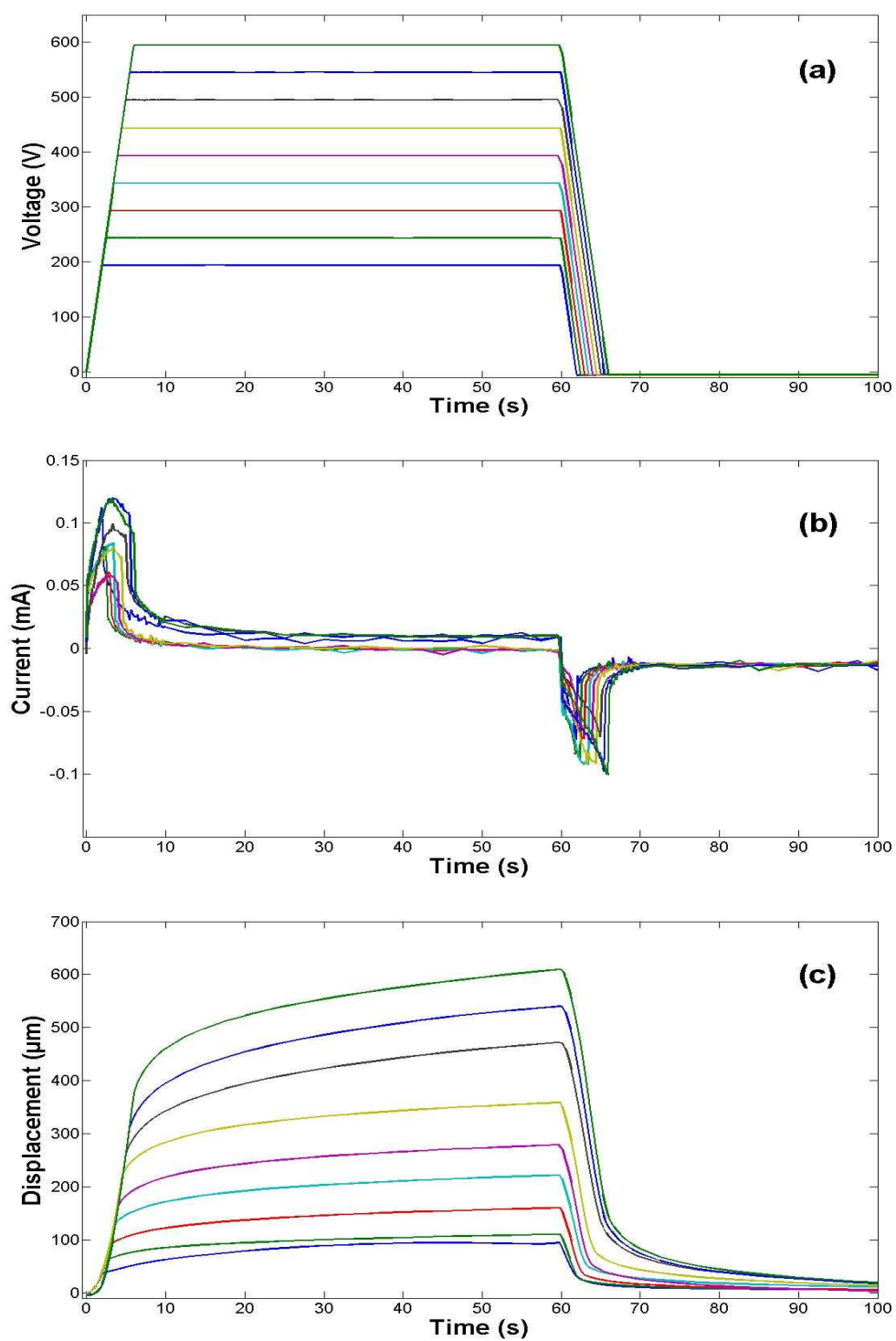


Figure C.11 Displacement characteristics of actuator #11 for voltages ranging from 200V to 600V. (a) Voltage vs. time. (b) Current vs. time. (c) Displacement vs. time.

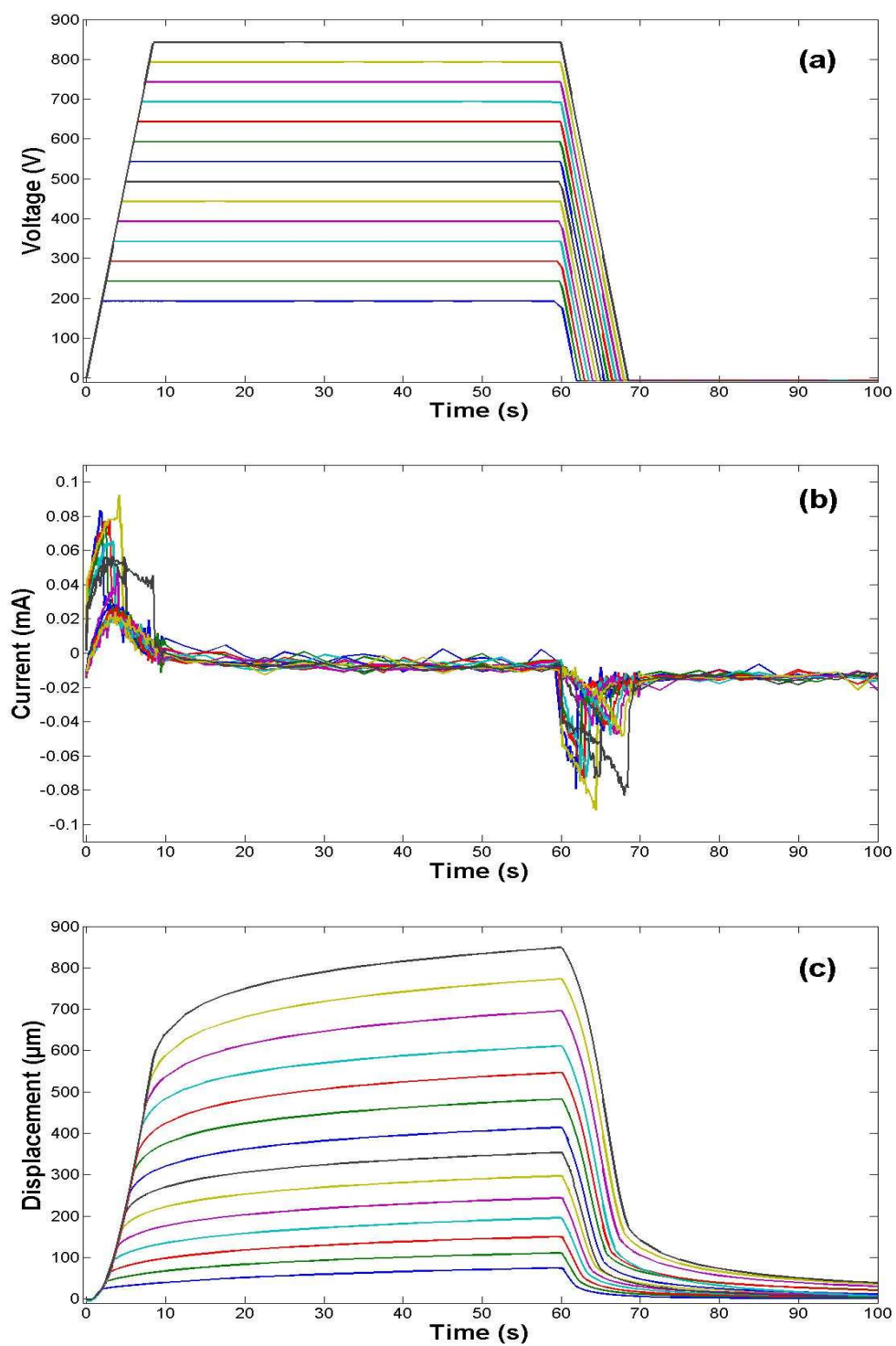


Figure C.12 Displacement characteristics of actuator #12 for voltages ranging from 200V to 850V. (a) Voltage vs. time. (b) Current vs. time. (c) Displacement vs. time.

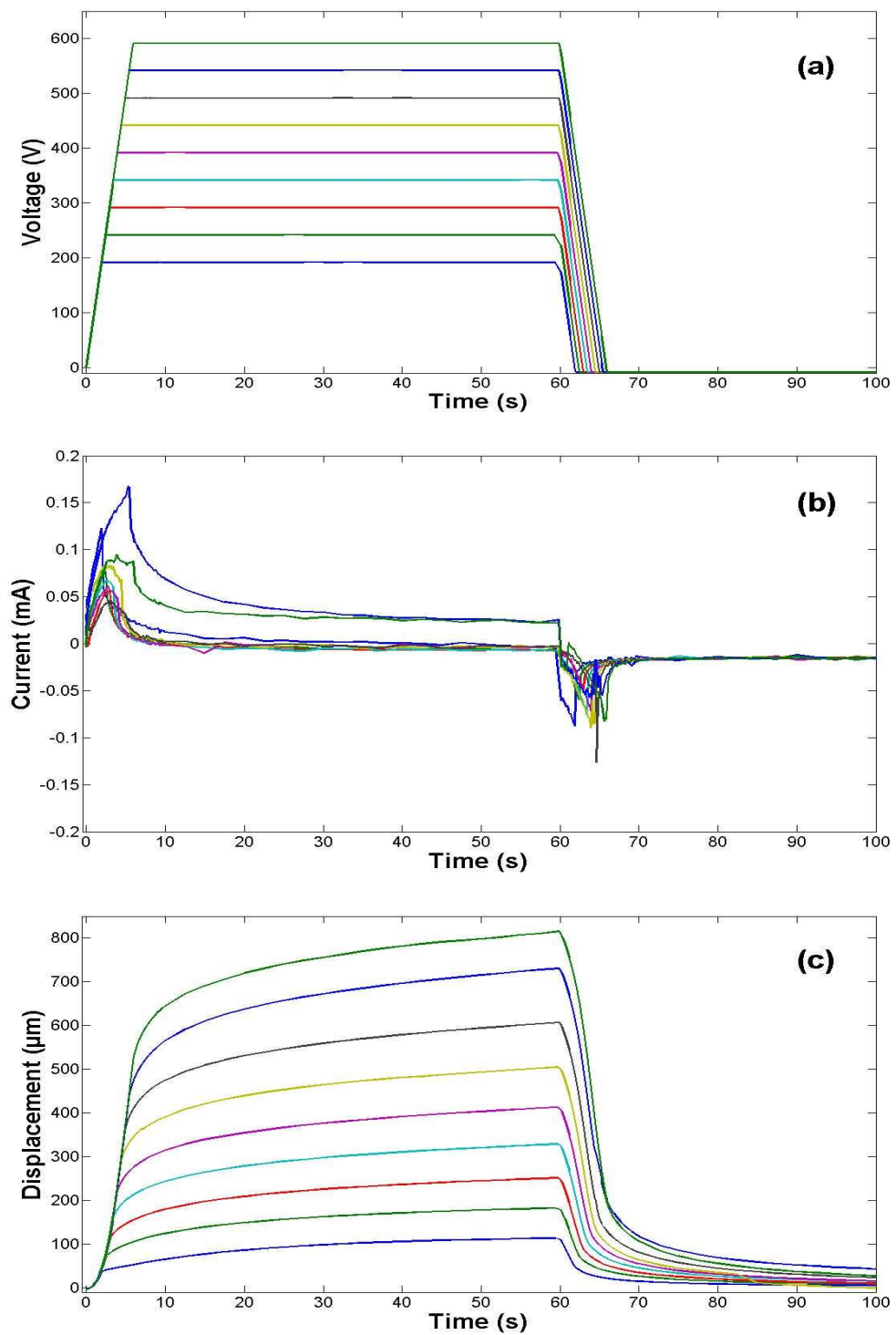


Figure C.13 Displacement characteristics of actuator #13 for voltages ranging from 200V to 600V. (a) Voltage vs. time. (b) Current vs. time. (c) Displacement vs. time.

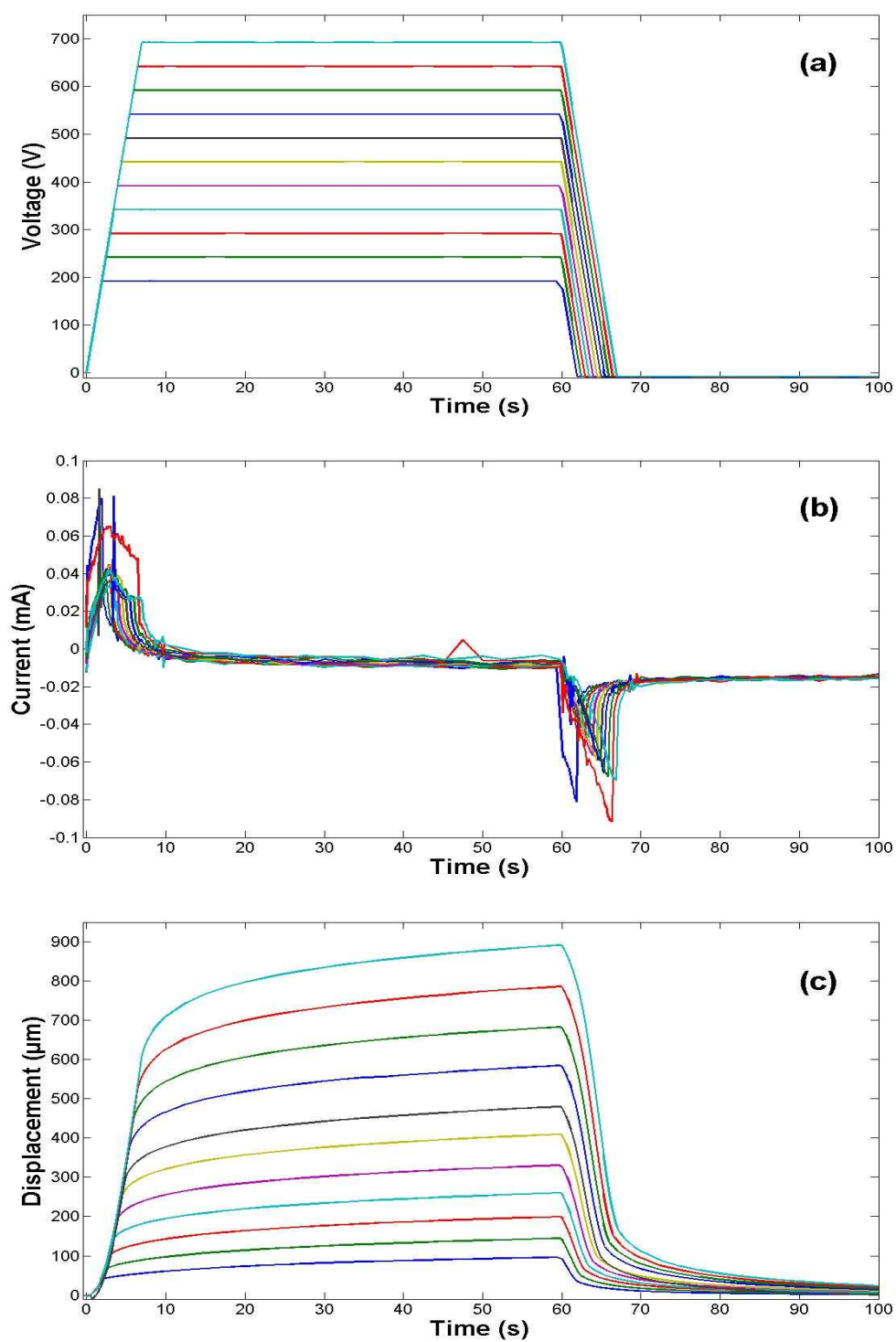


Figure C.14 Displacement characteristics of actuator #14 for voltages ranging from 200V to 700V. (a) Voltage vs. time. (b) Current vs. time. (c) Displacement vs. time.

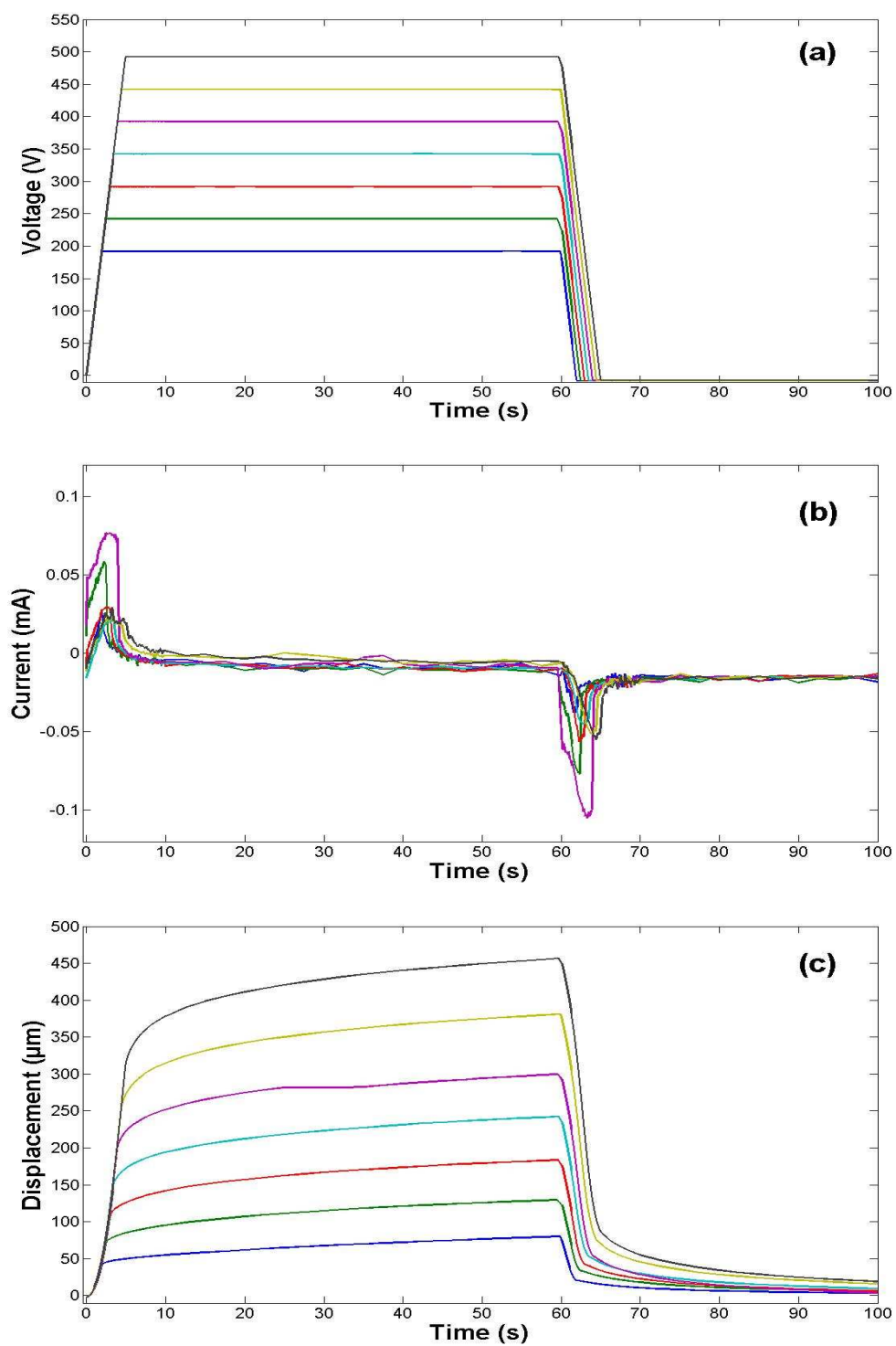


Figure C.15 Displacement characteristics of actuator #15 for voltages ranging from 200V to 500V. (a) Voltage vs. time. (b) Current vs. time. (c) Displacement vs. time.

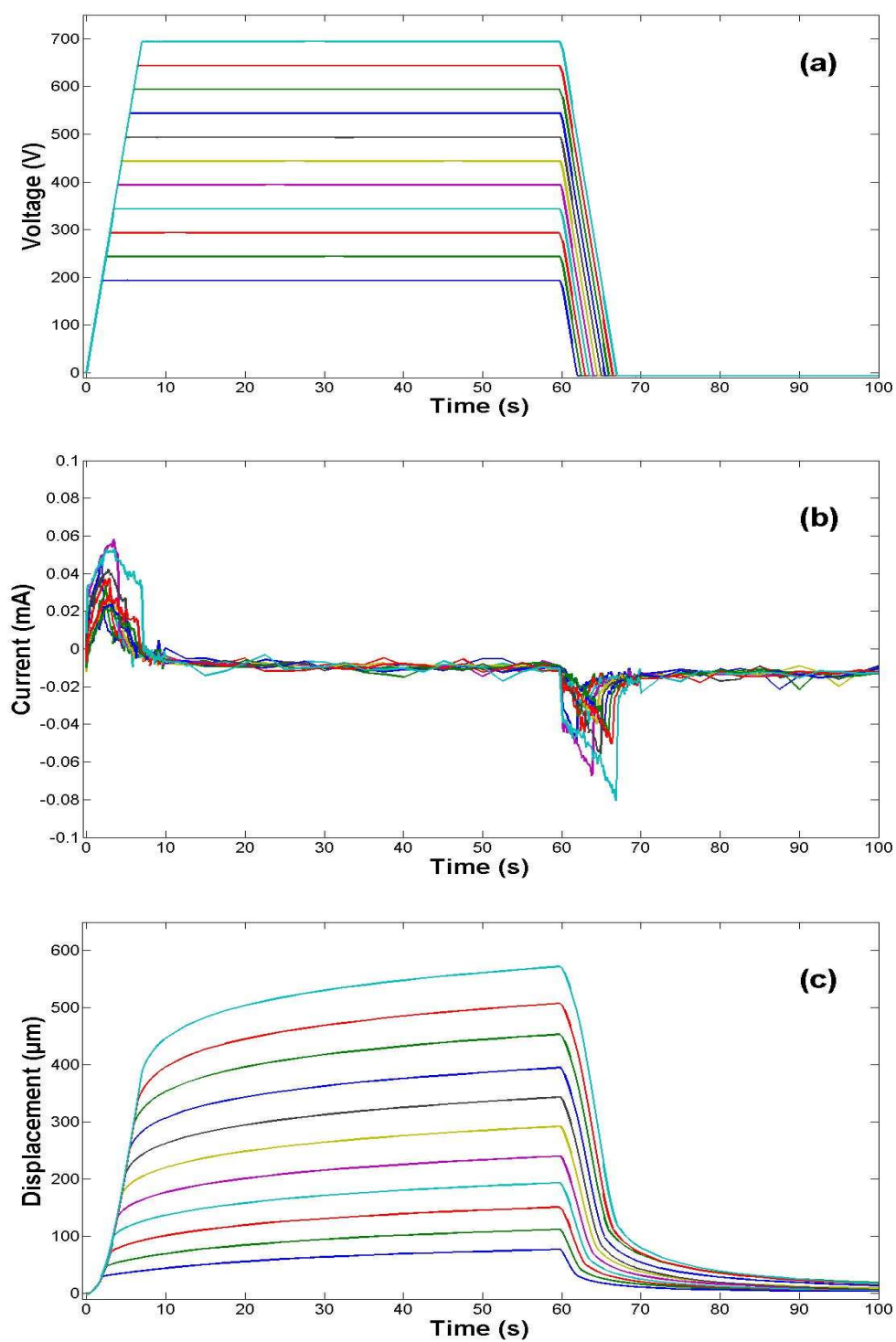


Figure C.16 Displacement characteristics of actuator #16 for voltages ranging from 200V to 700V. (a) Voltage vs. time. (b) Current vs. time. (c) Displacement vs. time.

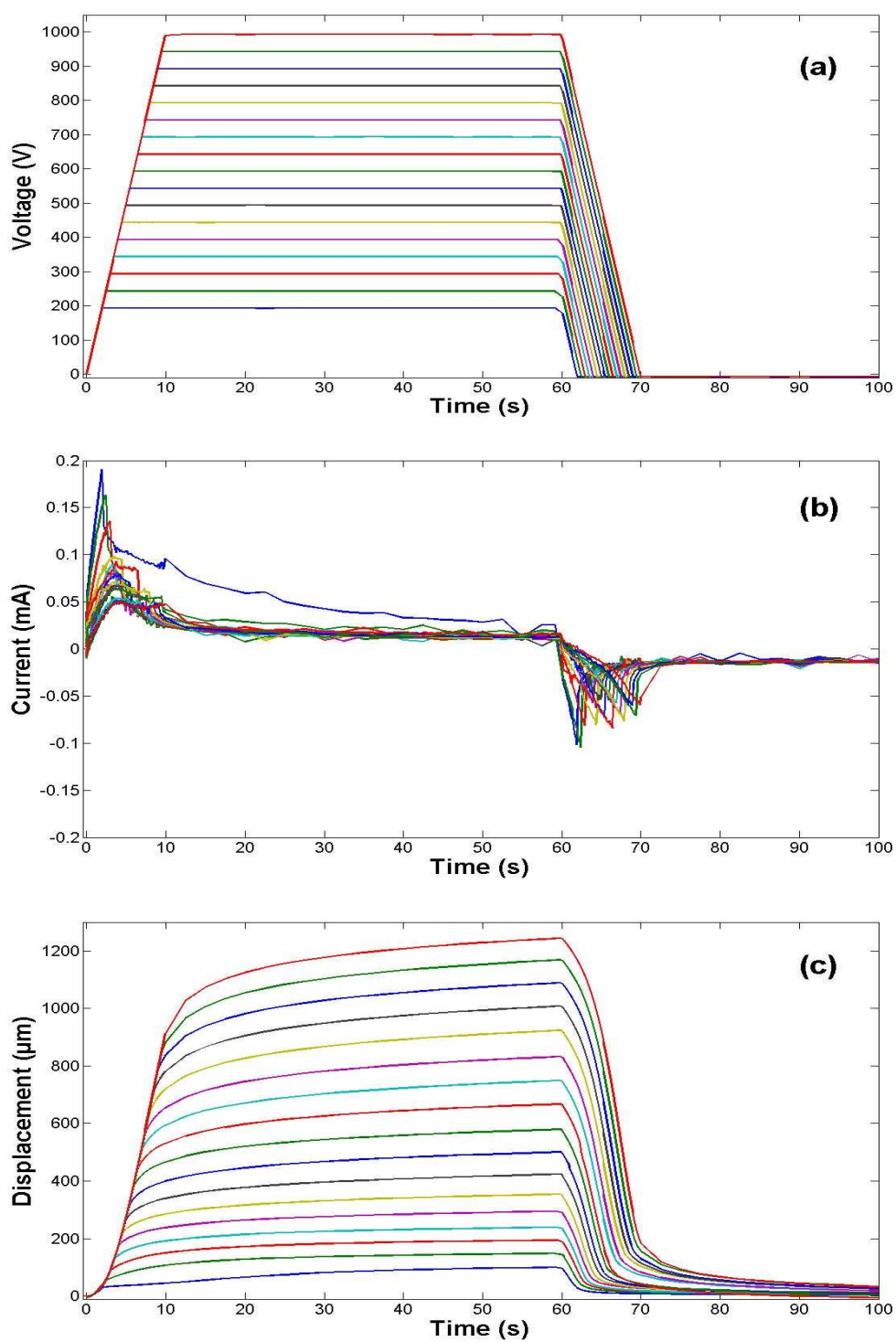


Figure C.17 Displacement characteristics of actuator #17 for voltages ranging from 200V to 1050V. (a) Voltage vs. time. (b) Current vs. time. (c) Displacement vs. time.

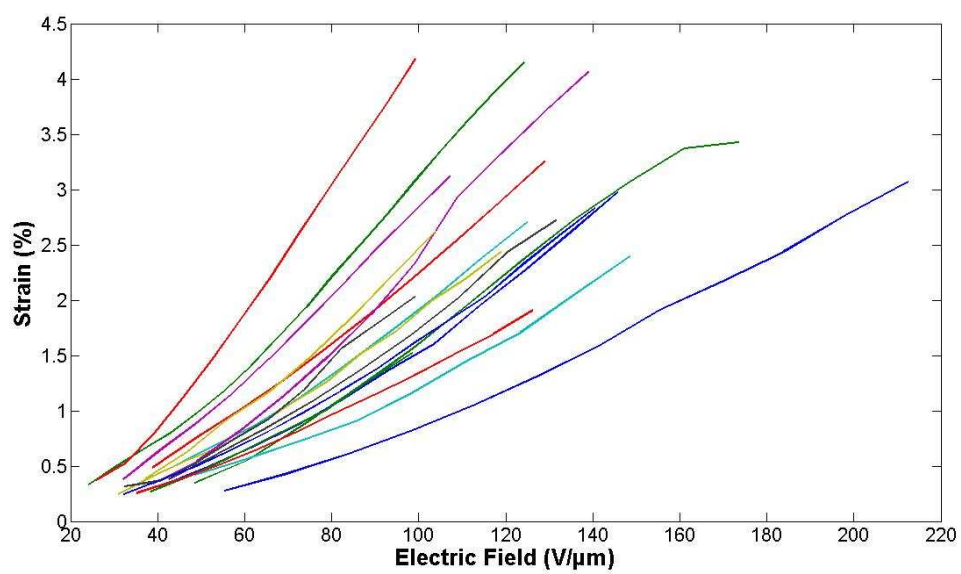


Figure C.18 Strain characteristics of all 17 actuators as a function of the applied electric field.

Appendix D

Force data of the PVDF actuators

In this section, we provide all the force measurements recorded for the 8 actuators that were tested using the cantilever beam load cell. Each figure shows the applied voltage and the force response, as a function of time. The input voltage was ramped at a rate of 100 V/s until reaching the desired value, to reduce the maximum current and avoid breakdown. Finally, Fig. D.8 shows the force vs. electric field for all samples, obtained by combining the force data, the applied voltage, and the bilayer thickness.

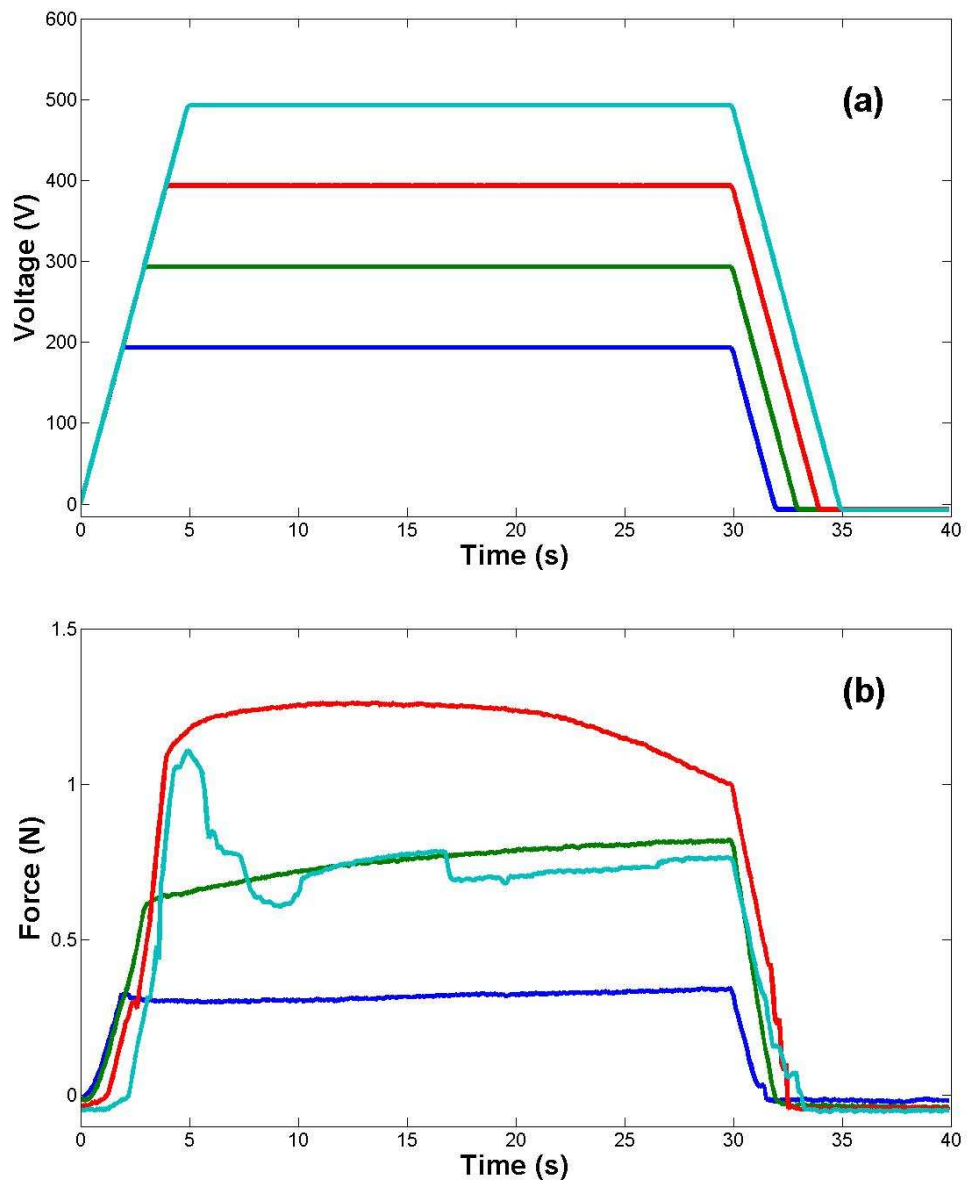


Figure D.1 Force characteristics of actuator #2 for voltages ranging from 200V to 500V. (a) Voltage vs. time. (b) Force vs. time.

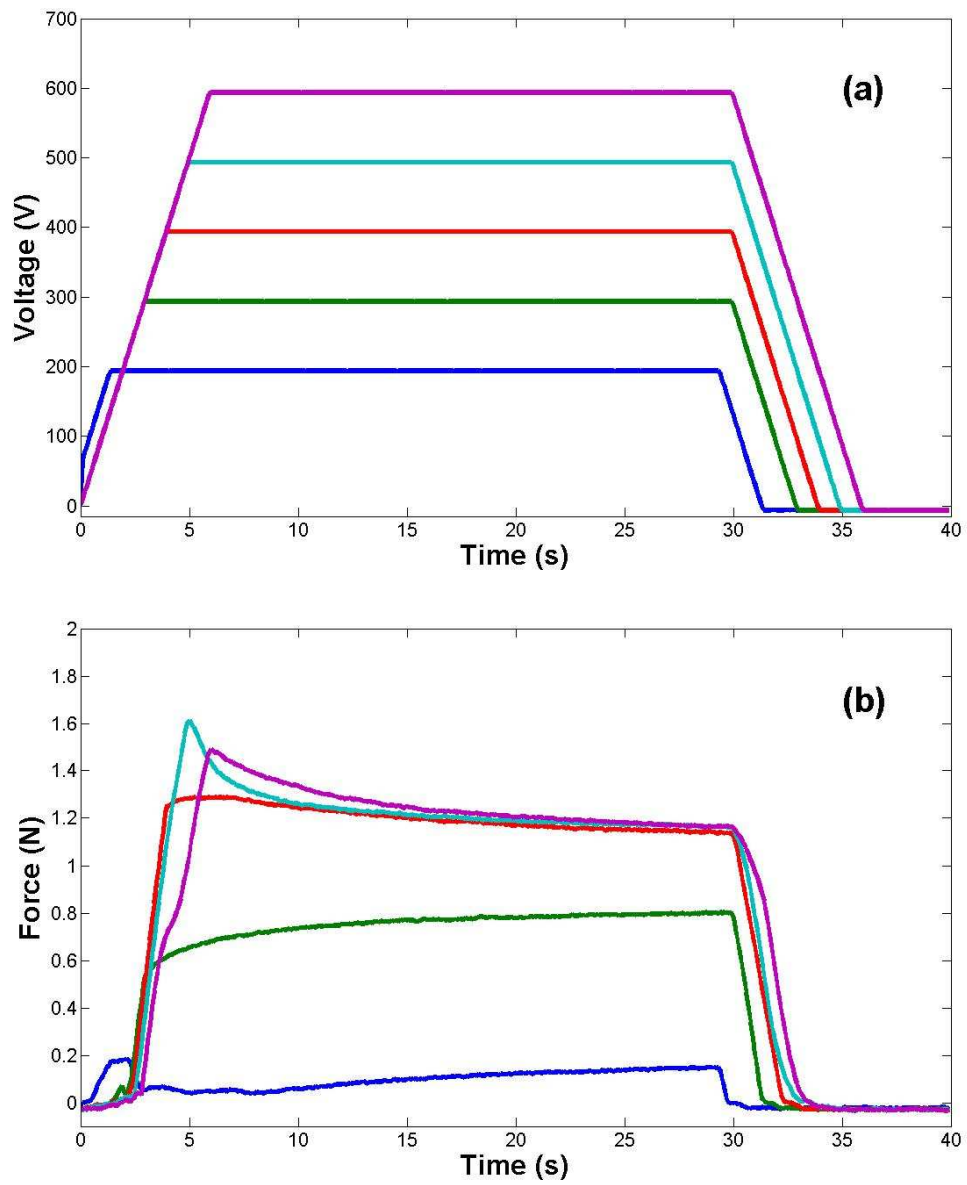


Figure D.2 Force characteristics of actuator #7 for voltages ranging from 200V to 600V. (a) Voltage vs. time. (b) Force vs. time.

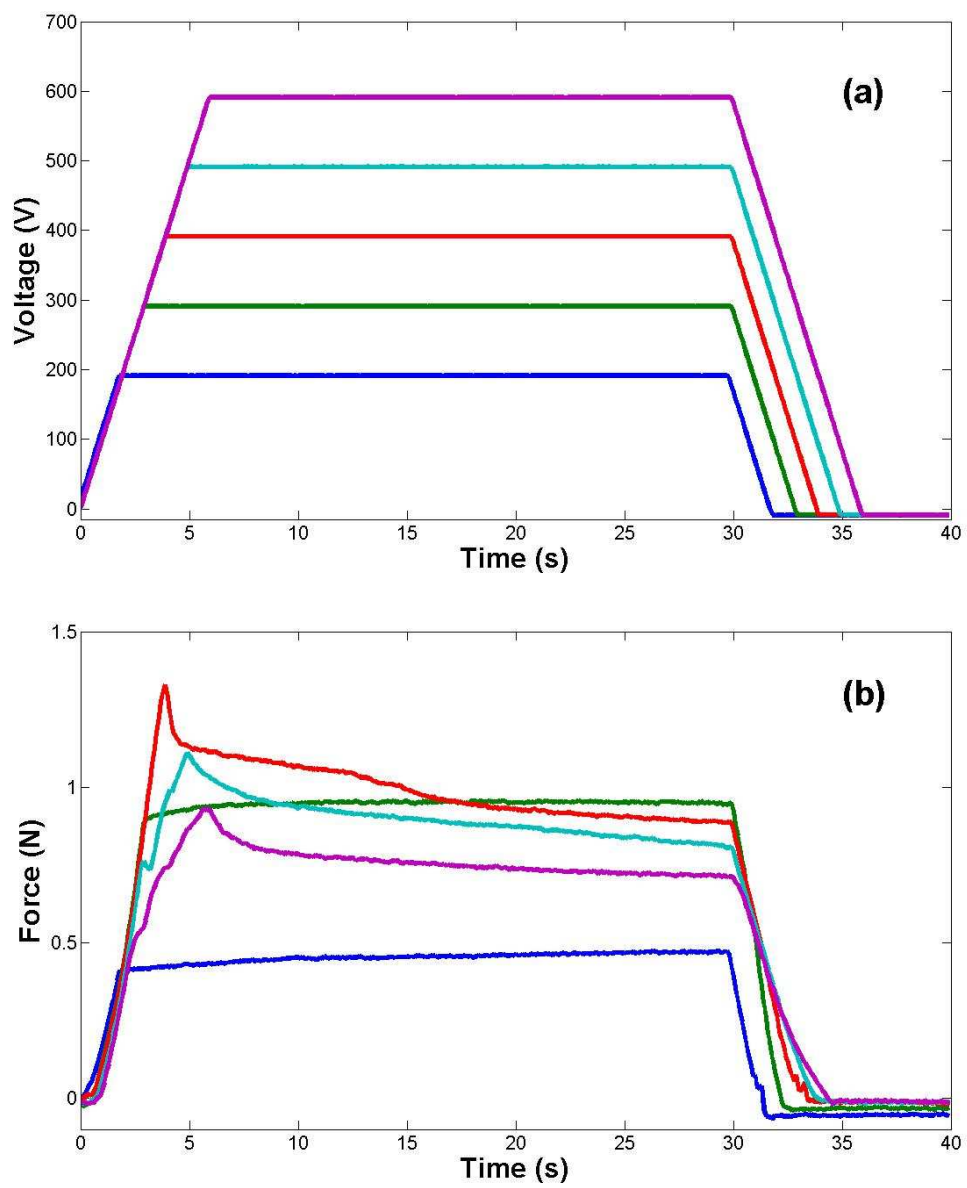


Figure D.3 Force characteristics of actuator #9 for voltages ranging from 200V to 600V. (a) Voltage vs. time. (b) Force vs. time.

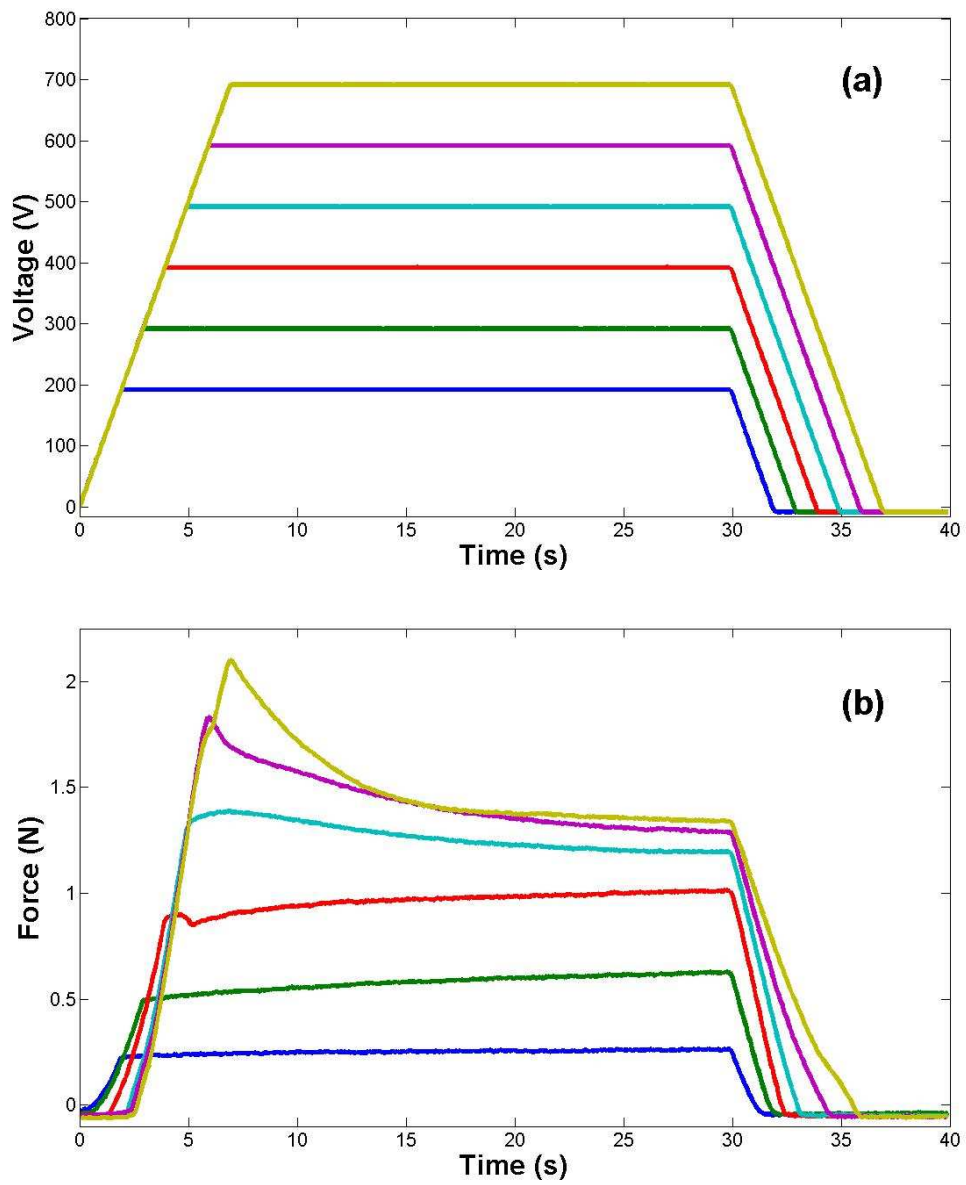


Figure D.4 Force characteristics of actuator #10 for voltages ranging from 200V to 700V. (a) Voltage vs. time. (b) Force vs. time.

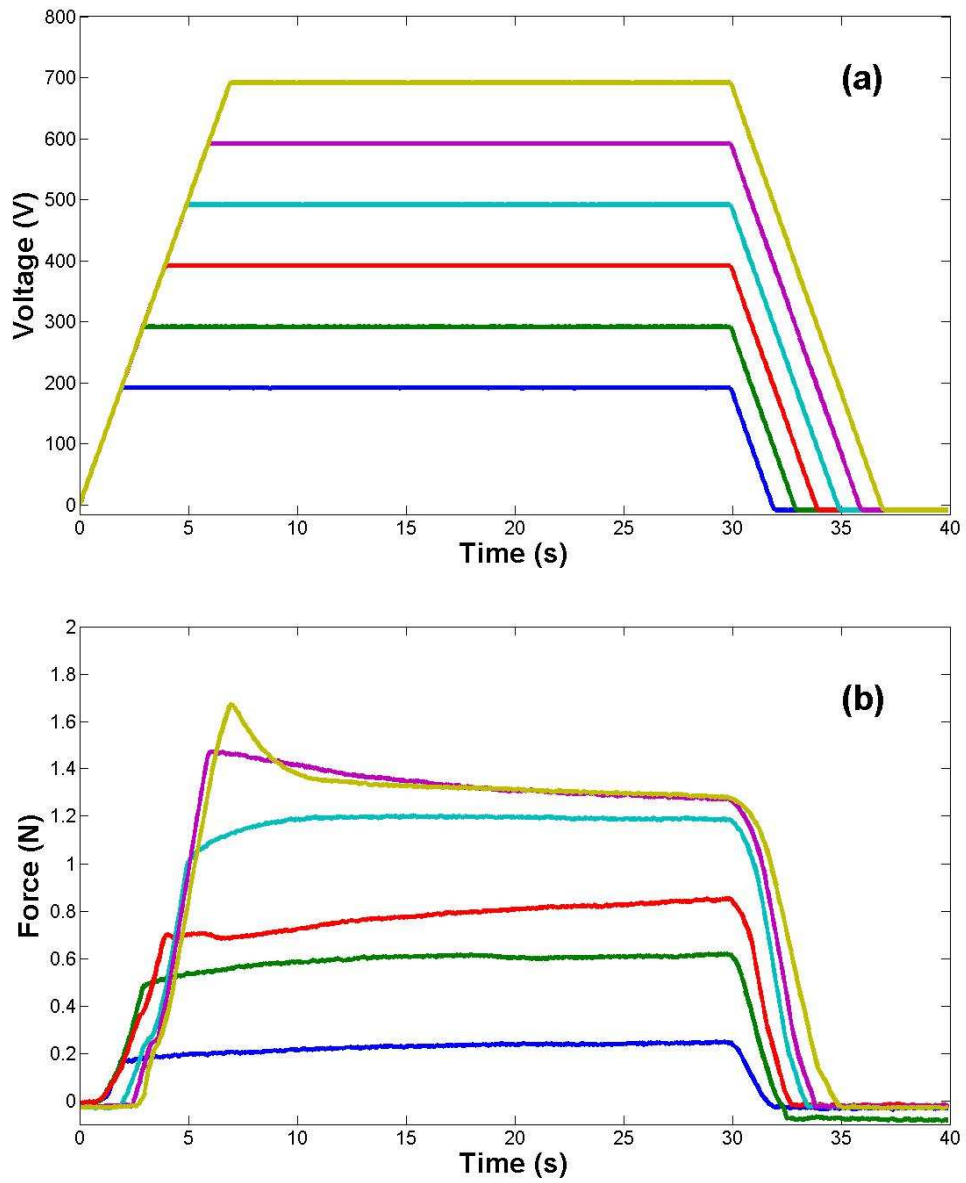


Figure D.5 Force characteristics of actuator #12 for voltages ranging from 200V to 700V. (a) Voltage vs. time. (b) Force vs. time.

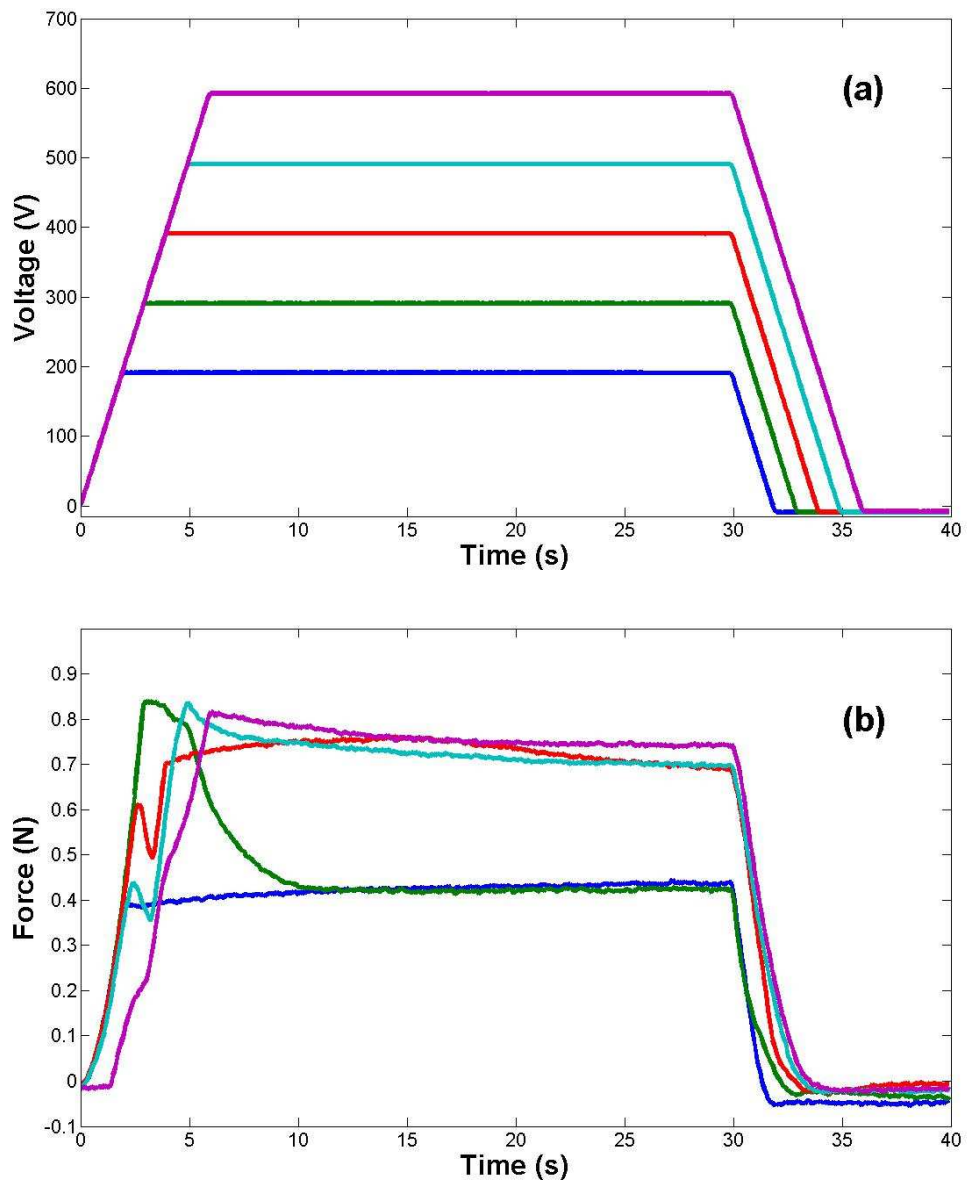


Figure D.6 Force characteristics of actuator #14 for voltages ranging from 200V to 600V. (a) Voltage vs. time. (b) Force vs. time.

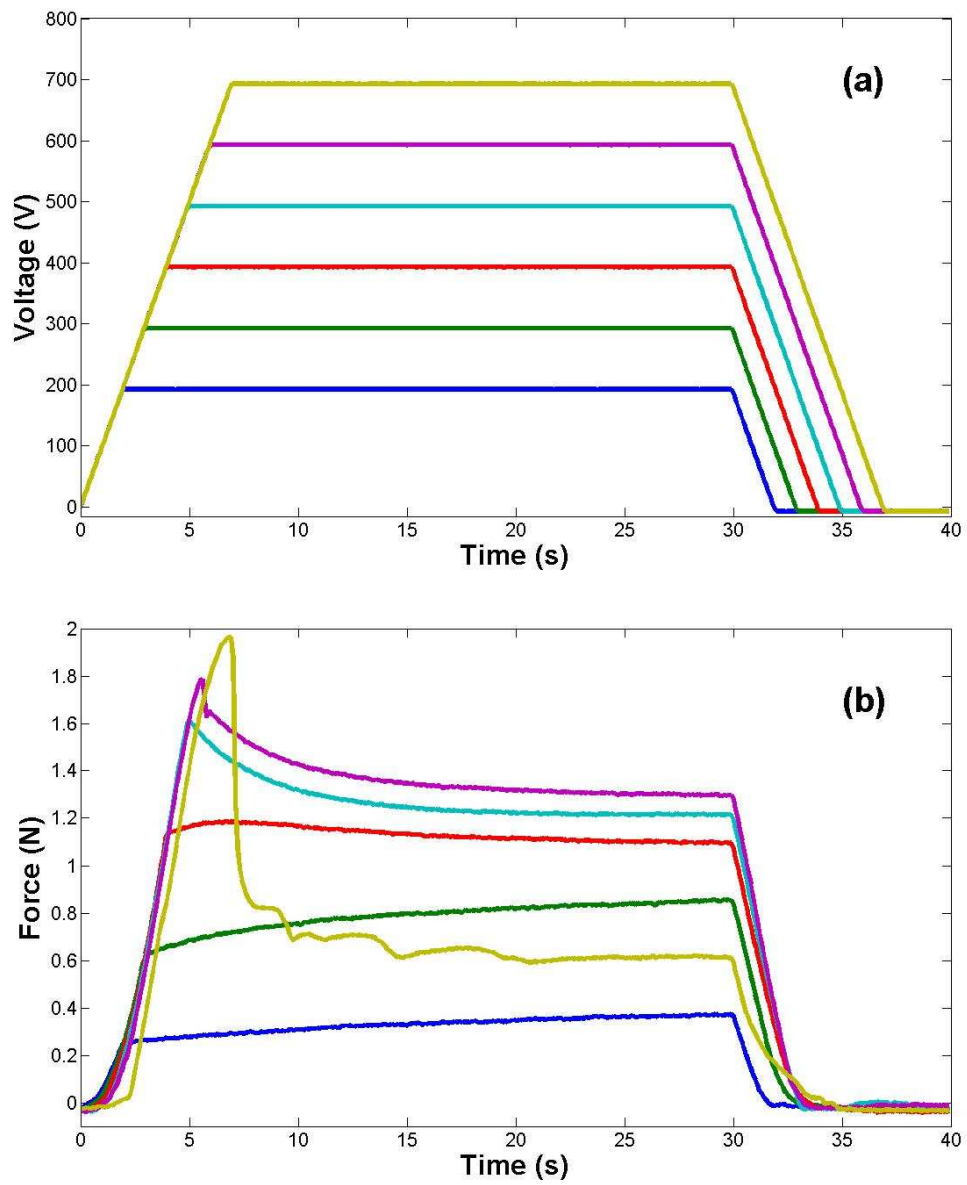


Figure D.7 Force characteristics of actuator #16 for voltages ranging from 200V to 700V. (a) Voltage vs. time. (b) Force vs. time.

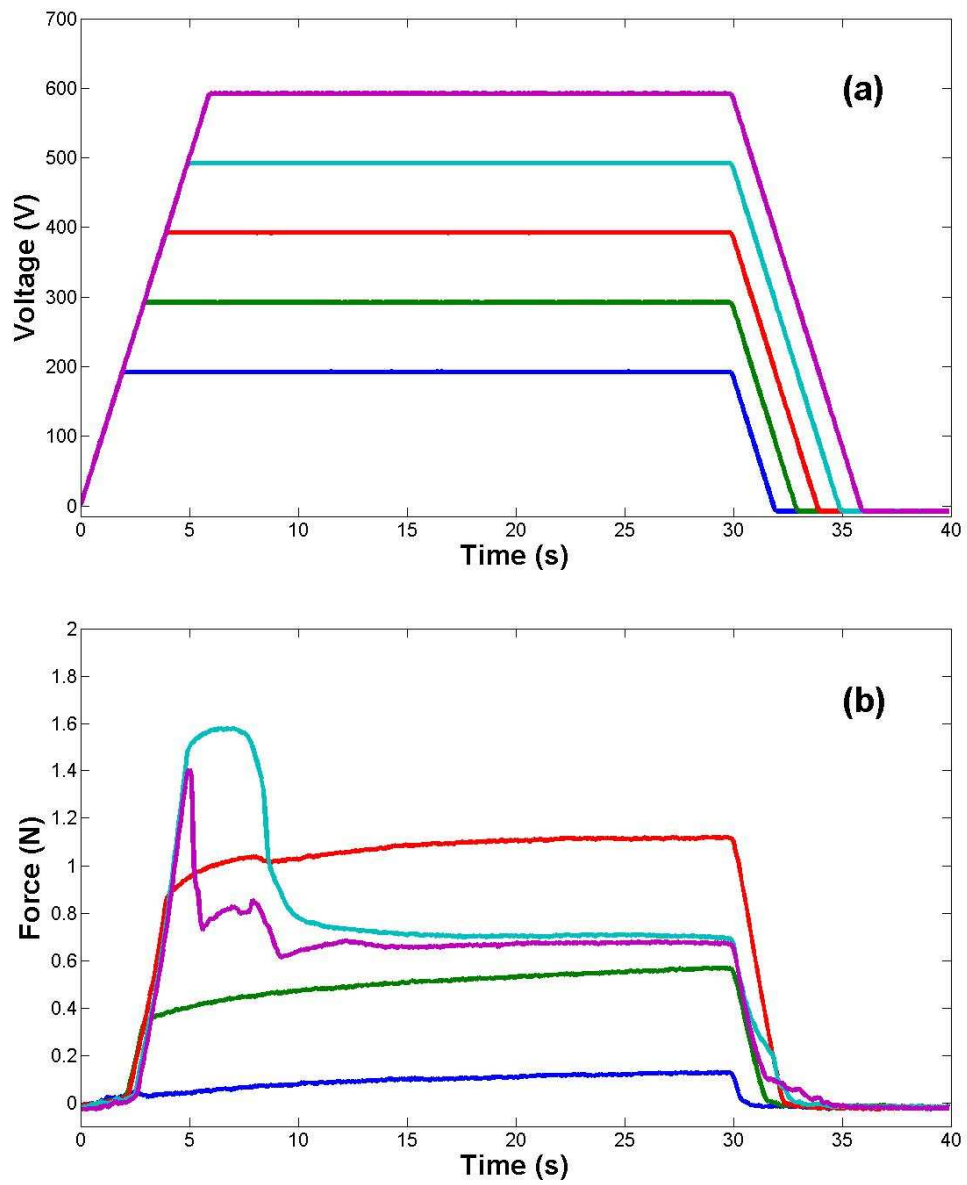


Figure D.8 Force characteristics of actuator #17 for voltages ranging from 200V to 600V. (a) Voltage vs. time. (b) Force vs. time.

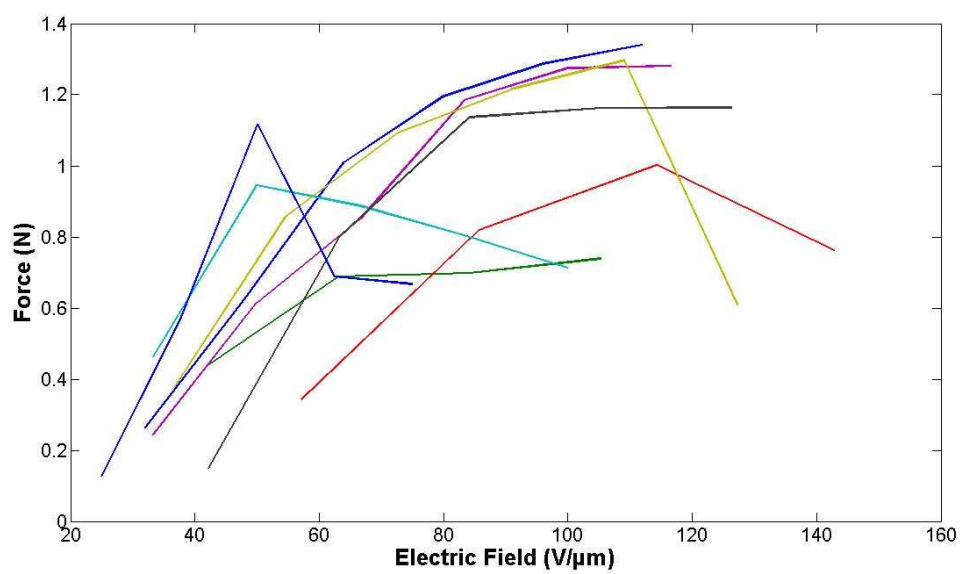


Figure D.9 Force characteristics of all 8 actuators as a function of the applied electric field.

Appendix E

Hysteresis and frequency response data of the PVDF actuators

In this section, we provide the hysteresis characteristics of actuator #9 for different frequencies at 600 V. This experiment was performed using a sine function as the input signal. In Fig. F.1 through F.7, notice the well know shape of a hysteresis curve: the charge and discharge of the actuator do not follow the same loading path. This is typical of a ferroelectric material. Finally, Fig. F.8 shows the frequency response of actuator #9 obtained from the hysteresis plots. The maximum displacement corresponds to the DC voltage case. The frequency gain drops drastically at low frequency because of the slow reversible effect of the actuator. Frequencies above 10 Hz were not tested, since the actuators fails near that value.

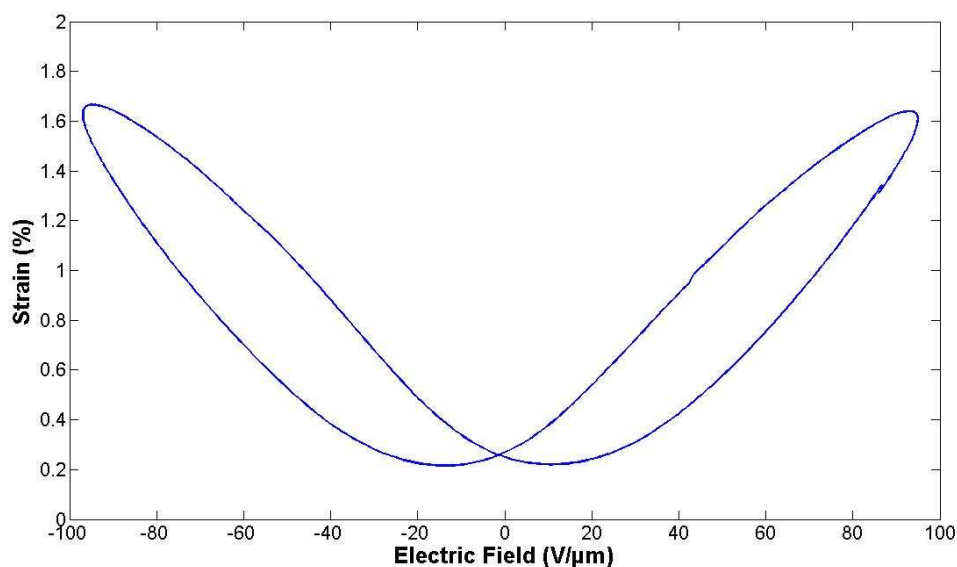


Figure E.1 Hysteresis characteristic of actuator #9 at 400 V and 0.1 Hz input sine wave.

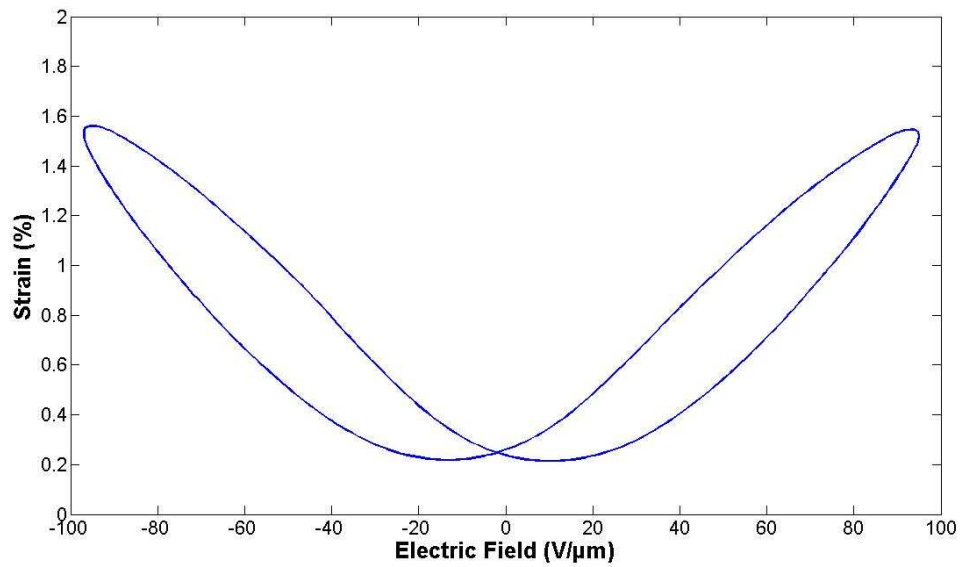


Figure E.2 Hysteresis characteristic of actuator #9 at 400 V and 0.25 Hz input sine wave.

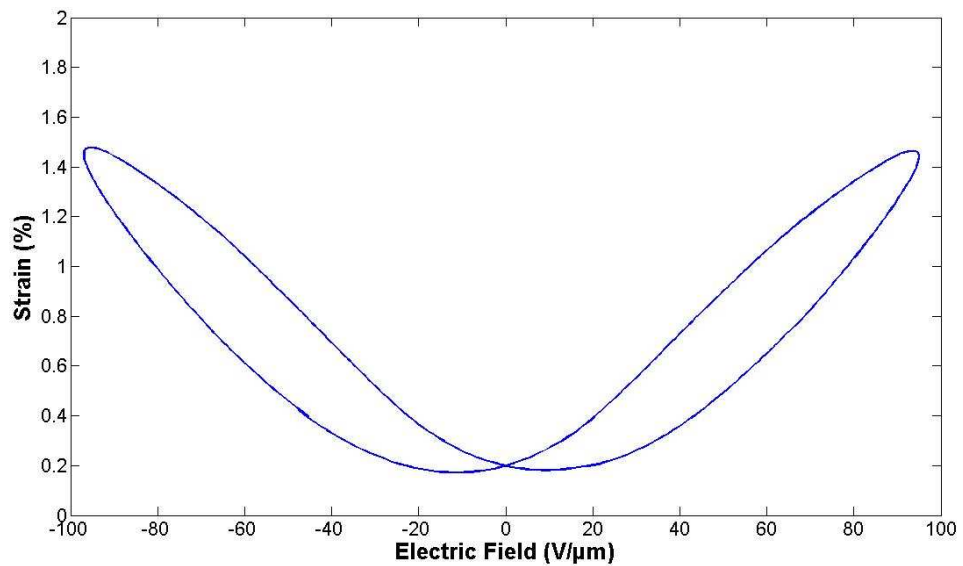


Figure E.3 Hysteresis characteristic of actuator #9 at 400 V and 0.5 Hz input sine wave.

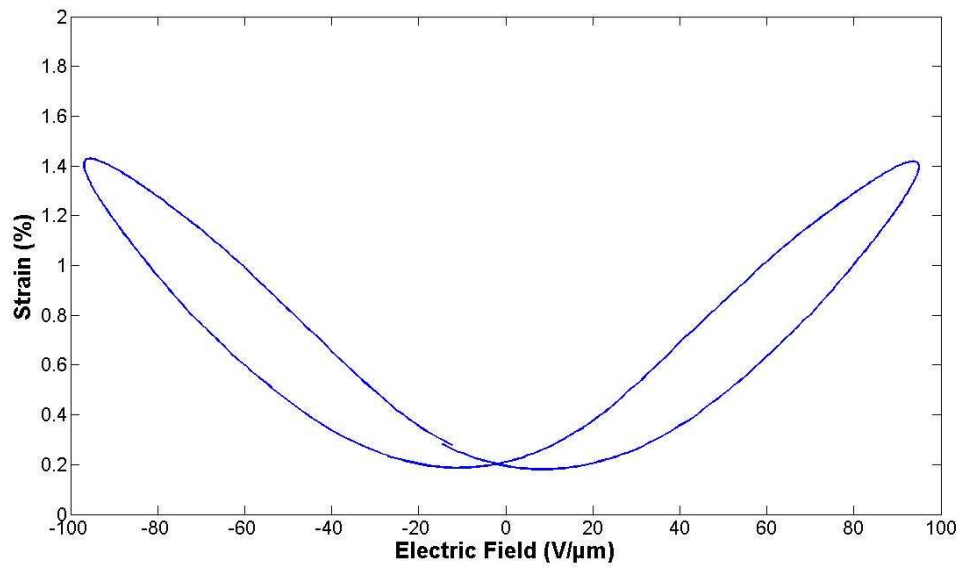


Figure E.4 Hysteresis characteristic of actuator #9 at 400 V and 1 Hz input sine wave.

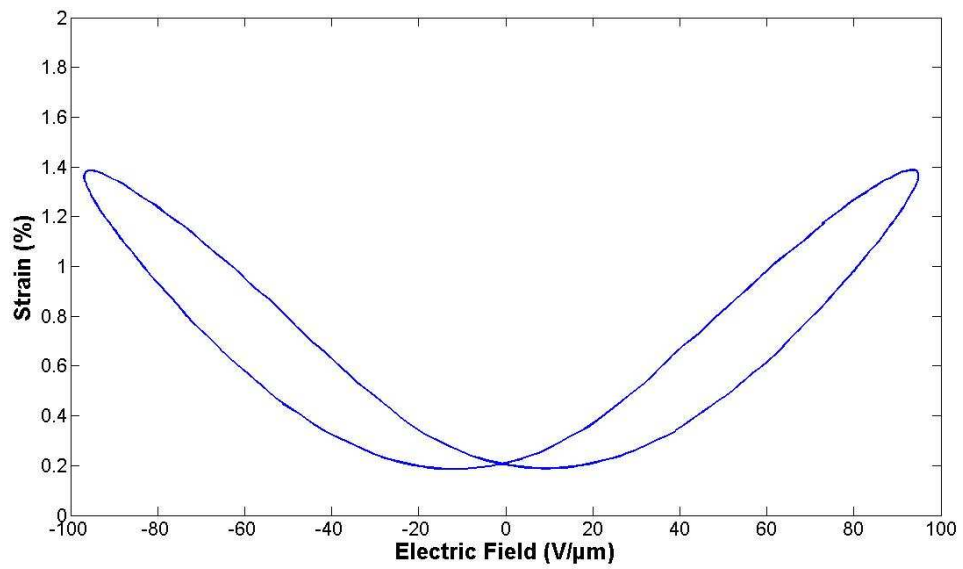


Figure E.5 Hysteresis characteristic of actuator #9 at 400 V and 2 Hz input sine wave.

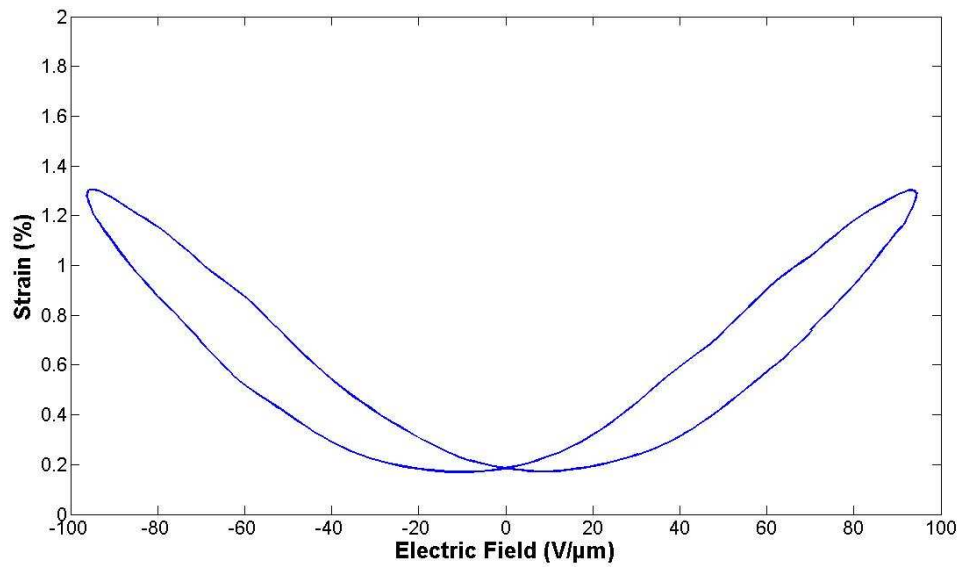


Figure E.6 Hysteresis characteristic of actuator #9 at 400 V and 5 Hz input sine wave.

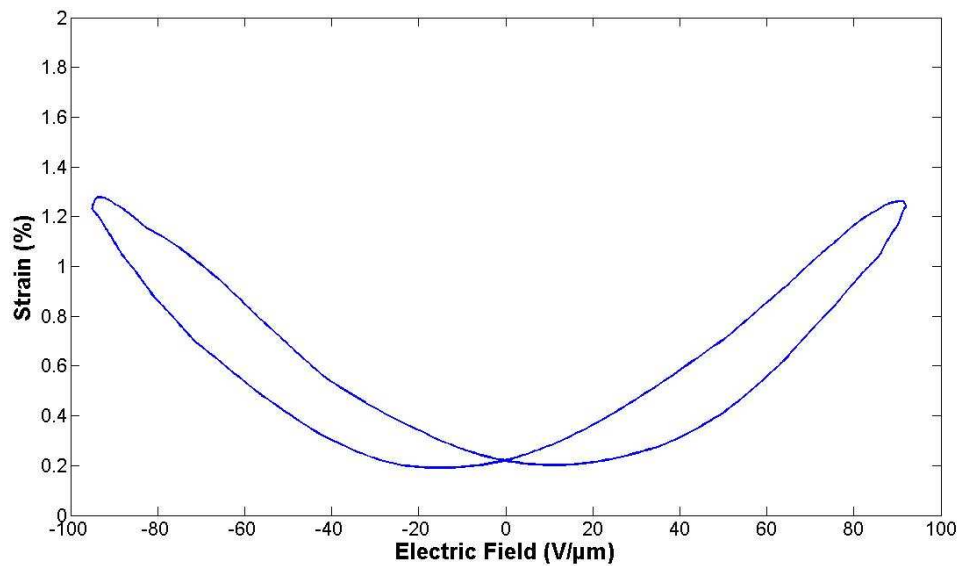


Figure E.7 Hysteresis characteristic of actuator #9 at 400 V and 10 Hz input sine wave.

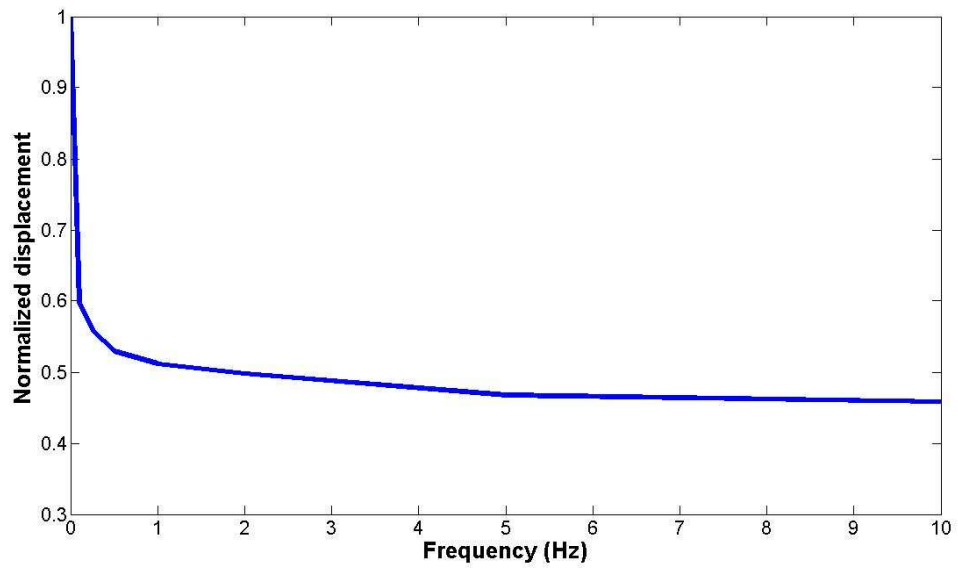


Figure E.8 Frequency response of actuator #9 at 400 V.

Appendix F

Temperature dependence data of the PVDF actuators

In this section, we provide the displacement measurements at 400 V for actuator #16 as a function of temperature. This experiment was performed to confirm that temperature could influence the strain performance of the device. The measurement cell was submerged in golden oil, and placed on a heat plate with temperature control. An increase in displacement of 35% was observed as temperature changed from 23°C to 40°C. We can conclude that a higher temperature increases the strain characteristics of the actuator, which is expected of PVDF based materials. More testing is needed to get the general strain vs. temperature response of the actuator.

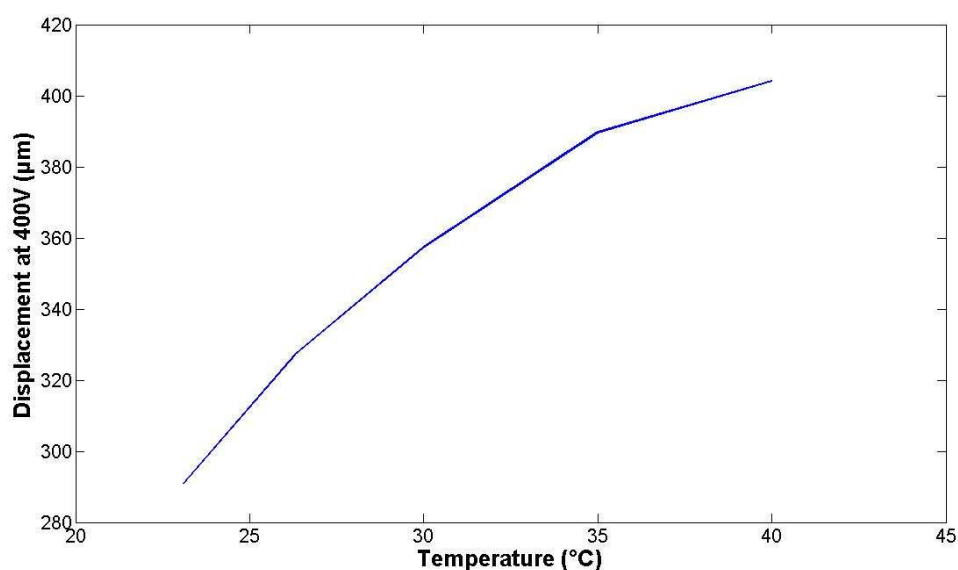


Figure F.19 Displacement characteristics of actuator #16 at 400V as a function of temperature.